

Water Resources Research

RESEARCH ARTICLE

10.1029/2017WR022464

Key Points:

- Pleistocene glaciations can cause geomechanical failure, permeability increases, and brine flushing within sedimentary basin aquifers
- To reconcile computed and observed underpressures within confining units, failure must occur along discrete fracture planes through shales
- Simulated Holocene-Modern overpressure beyond the ice sheet terminus could help to explain failure and seismicity in the basement

Supporting Information:

- Supporting Information S1
- Data Set S1

Correspondence to:

M. Person,
mperson@nmt.edu

Citation:

Zhang, Y., Person, M., Voller, V., Cohen, D., McIntosh, J., & Grapenthin, R. (2018). Hydromechanical impacts of Pleistocene glaciations on pore fluid pressure evolution, rock failure, and brine migration within sedimentary basins and the crystalline basement. *Water Resources Research*, 54. <https://doi.org/10.1029/2017WR022464>

Received 21 DEC 2017

Accepted 23 JUL 2018

Accepted article online 30 AUG 2018

Hydromechanical Impacts of Pleistocene Glaciations on Pore Fluid Pressure Evolution, Rock Failure, and Brine Migration Within Sedimentary Basins and the Crystalline Basement

Yipeng Zhang¹ , Mark Person¹ , Vaughan Voller² , Denis Cohen¹ , Jennifer McIntosh³ , and Ronni Grapenthin¹ 

¹Department of Earth and Environmental Sciences, New Mexico Tech, Socorro, NM, USA, ²Department of Civil, Environmental, and Geo-Engineering, University of Minnesota, Minneapolis, MN, USA, ³Department of Hydrology and Atmospheric Sciences, University of Arizona, Tucson, AZ, USA

Abstract The effects of Pleistocene glacial loading on rock failure, permeability increases, pore pressure evolution, and brine migration within two linked sedimentary basins were evaluated using a multiphysics control volume finite element model. We applied this model to an idealized cross section that extends across the continent of North America from the Hudson Bay to the Gulf of Mexico. Our analysis considered lithosphere geomechanical stress changes ($\sigma_{yy} > 35$ MPa) in response to 10 cycles of ice sheet loading. Hydrologic boundary conditions, lithosphere rheological properties, and aquifer/confining unit configuration were varied in a sensitivity study. We used a Coulomb Failure Stress change metric ($\Delta\text{CFS}_p > 0.1$ MPa) to increase permeability by a factor of 100 in some simulations. Results suggest that a buildup of anomalous pore pressures up to about 3 MPa occurred in confining units during periods of glaciations, but this had only a second-order effect on triggering rock failure. In regions prone to failure, permeability increases during glaciations help to explain observations of brine flushing in sedimentary basin aquifers. During the Holocene to present day, deglaciation resulted in underpressure formation in confining units primarily along the northern margin of the northern basin. Holocene-modern geomechanical stress fields were relatively small (<0.6 MPa). However, pore pressure increases associated with postglacial rebound, especially when a basal sedimentary basin aquifer is present, induced rock failure and seismicity up to 150 km beyond the terminus of the ice sheet. Sedimentary basin salinity patterns did not equilibrate after 10 simulated glacial cycles.

1. Introduction

A key requirement for high-level nuclear waste repository siting is to ensure that future groundwater flow systems do not transport radionuclides into shallow potable aquifers for up to 10^5 or 10^6 years (Bredehoeft et al., 1978; De Marsily, 1986; Person et al., 2012). Most studies (Talbot, 1999; Walker & Kasting, 1992), though not all (Archer & Ganopolski, 2005), conclude that for countries at high latitude, the specter of future glaciations within the next 10–20 thousand years seems inevitable. Hydrogeological reconstructions of past glaciations suggest that continental ice sheet loading resulted in the formation of anomalous pressures in tight confining units ($<10^{-20}$ m²; Neuzil, 2013; Neuzil & Provost, 2014; Vinard et al., 1993, 2001), induced reversals in regional subsurface flow directions (Bense & Person, 2008; Grasby et al., 2000), and increased groundwater flow rates by about 1 order of magnitude above interglacial levels (Lemieux et al., 2008a). Geochemical tracers suggest that large volumes of glacial meltwater were emplaced along the northern margins of continental sedimentary basins across North America (McIntosh et al., 2012; Schlegel et al., 2011; Siegel, 1991; Siegel & Mandel, 1984) and Europe and along the continental shelf (Cohen et al., 2010; Person et al., 2003; Siegel et al., 2014).

Prior assessments of the effects of glaciation on nuclear waste isolation in countries such as Switzerland, Sweden, Canada, and France have focused primarily on enhanced erosion rates (Cohen, 2015; Hallet, 2011; Iverson & Person, 2012), seismicity due to mechanical loading (Arvidsson, 1996; Johnston et al., 1998; Klemann & Wolf, 1998; Lund, 2015), formation of anomalous pore pressures (Khader & Novakowski, 2014; Neuzil & Provost, 2014; Vinard et al., 1993, 2001), and diffusive transport of geochemical and isotopic tracers through tight argillaceous formations into adjacent, partially flushed reservoirs (Hendry et al., 2013, 2015;

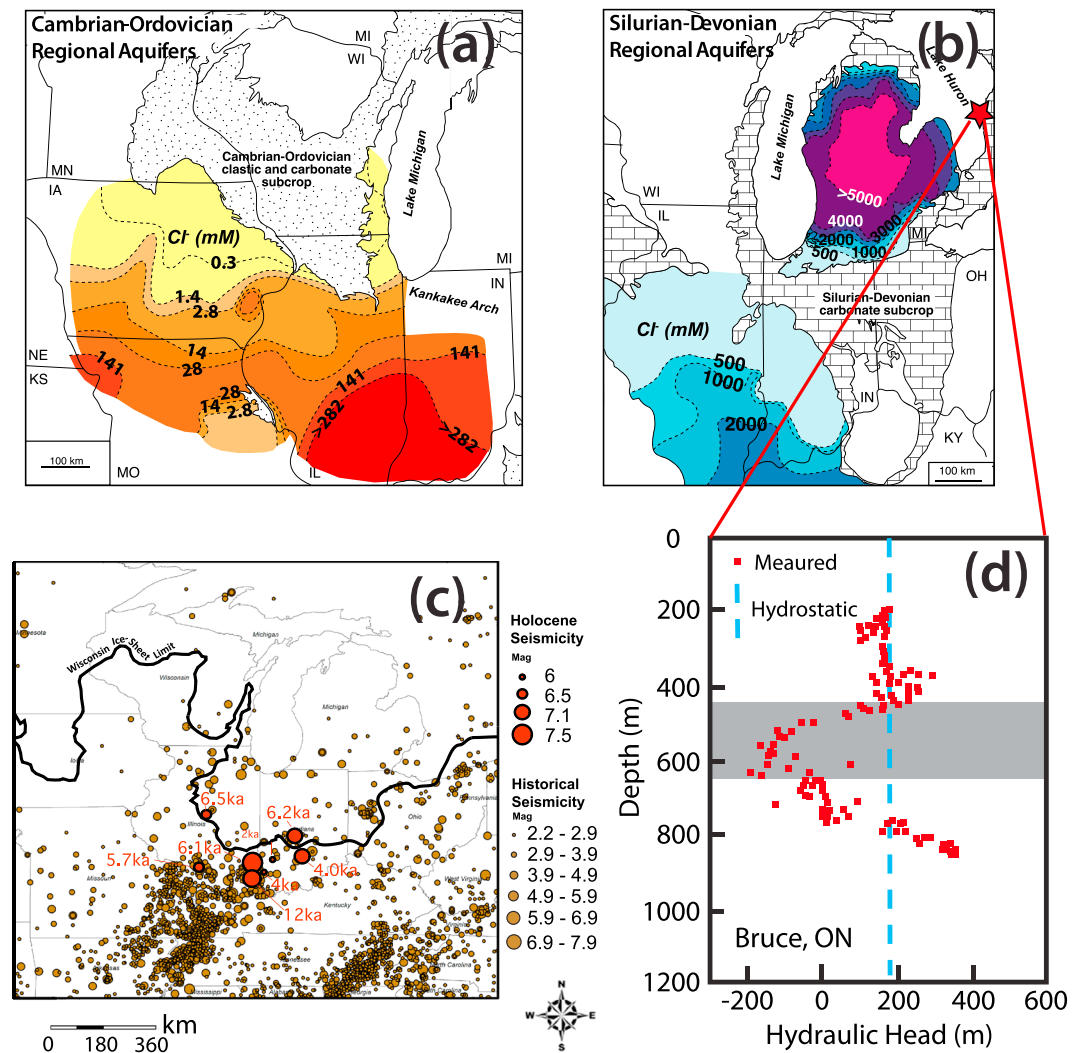


Figure 1. Contour maps depicting asymmetric salinity patterns (Cl^- in mM) within (a) midcontinental Cambro-Ordovician (after Person et al., 2007) and (b) Silurian-Devonian aquifers systems (after Person et al., 2007). (c) Epicenters of holocene seismicity (red circles, from Wheeler & Cramer, 2002) and historical earthquake (brown circles, NRC seismic source characterization project: <http://www.ceus-ssc.com>) compared with ice sheet margin delineated by a black line. (d) Anomalous (negative) fossil pore pressure preserved in the tight confining unit at the Bruce Site, Ontario. (Neuzil & Provost, 2014. The location of the Bruce site is shown in Figure 1b).

Mazurek et al., 2011). While Boulton and Caban (1995) and Neuzil (2012) noted the potential linkages between anomalous pore pressure and geomechanical failure associated with ice sheet loading, we are not aware of any study that has analyzed the role of pore pressure increases on triggering shear failure along critically stressed faults/fractures, as well as associated permeability increases during glaciations, and how this might influence brine flushing by meltwater incursion in sedimentary basin aquifers and confining units.

The most direct evidence that Pleistocene glacial loading has modified groundwater flow conditions comes from underpressure data collected within tight argillaceous formations in basins that were formerly glaciated. Within the midcontinent of North America, underpressures as low as 300 m below hydrostatic conditions have been measured in fine-grained carbonate rocks near Bruce, Ontario (Neuzil & Provost, 2014; Figure 1d). These tight Ordovician age deposits have very low measured permeability ($<10^{-21} \text{ m}^2$; data source: Neuzil & Provost, 2014; Walsh, 2011). The underpressures cannot be explained by erosional unloading, as midcontinent erosion rates are significantly lower than deglaciation rates. Similar anomalous pore pressures and ultralow-permeability conditions are also observed in Cretaceous argillaceous marls at the Wellenberg in Switzerland, where the borehole pressures are measured to be as low as 700 m below the hydrostatic

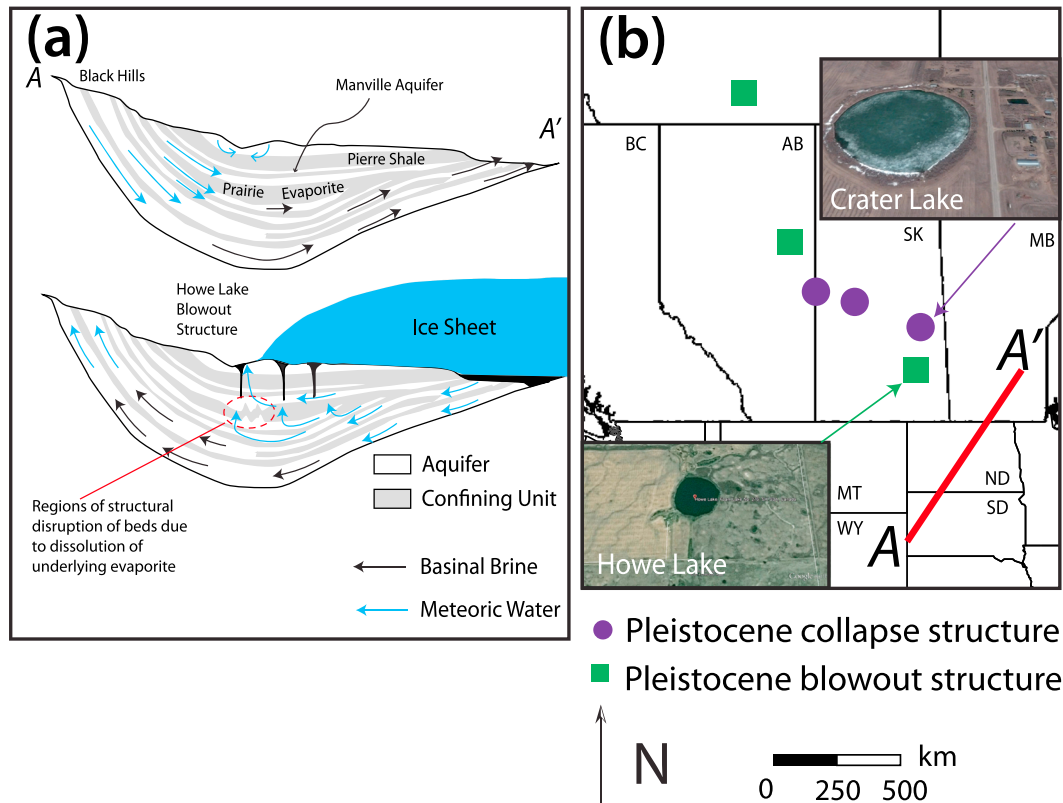


Figure 2. (a) Cross section illustrating the hypothesized origin and evolution of Howe Lake as a blow out structure due to ice sheet-induced excess fluid pressures (after Christiansen et al., 1982; Grasby et al., 2000) and the location of Howe Lake relative to the retreating ice sheet shortly after deglaciation began. (b) Base map shows the locations of Howe Lake along with other dissolution features and cross section A-A' in Figure 2a (after Grasby & Chen, 2005).

conditions (Vinard et al., 1993, 2001). These data sets are rare because of the great difficulty, expense, and time required to measure pressures in ultralow-permeability rocks. Within aquifers of the Michigan Basin, modest overpressures have been attributed to glacial loading (Bahr et al., 1994).

Additional evidence of the impact of continental ice sheets on subsurface flow patterns within sedimentary basins comes from geochemical and isotopic data sets. Siegel and Mandle (1984) and McIntosh and Walter (2006) noted that abnormal low-salinity conditions occur within the Cambrian-Ordovician (Figure 1a) and Devonian-Silurian (Figure 1b) aquifer systems in northeastern and central Iowa in formerly glaciated areas. Grasby et al. (2000) reported isotopic evidence of glacial meltwater incursion within formerly glaciated portions of the Williston Basin. Schlegel et al. (2011) reported that the New Albany Shale in the glaciated northern half the Illinois basin had anomalously low salinity levels (i.e., $0.5 M < \text{chloride}$) presumably caused by Pleistocene glacial meltwater incursion (Figure 1c). All of these formerly glaciated basins have an asymmetric salinity pattern within either aquifers or confining units whereby the northern side of the basin has lower concentrations than the southern half (Martini et al., 1998; McIntosh et al., 2012).

Other evidence suggesting glacial meltwater intrusion deep (>500 m) into the subsurface comes from studies of the dissolution of the Prairie Evaporite in the West Canada Sedimentary Basin (Figure 2). We hypothesize that reactivation of preexisting faults (shear failure) will provide high permeable flow channels for the fresh glacial meltwater, facilitating the evaporite dissolution. Collapse structures (denoted by purple circles, e.g., Crater Lake) and blow out structures (denoted by green squares, e.g., Howe Lake) shown in Figure 2b across West Canada Sedimentary Basin are all believed to be related to the dissolution of the Prairie Evaporite according to Christiansen et al. (1982), Grasby and Chen (2005), and Hendry et al. (2013). The collapse structures are direct consequences of the dissolution of this midlevel evaporite (Christiansen, 1967; Christiansen & Sauer, 2001; Gendzwill & Hajnal, 1971), while the genesis of blow out structures is relatively complex. Underlying Prairie Evaporite dissolution caused structural disruptions of the Manville

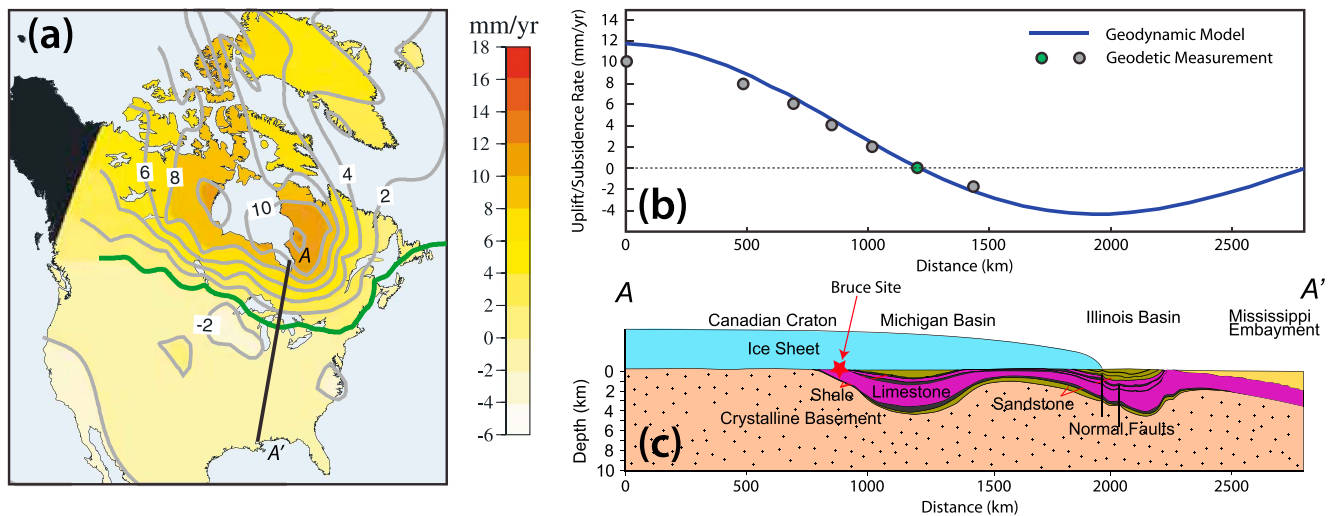


Figure 3. (a) Contour map of postglacial rebound rates across North America and location of the hinge line (i.e., zero uplift) that is indicated by the green bold line (after Sella et al., 2007). Line A-A' indicates the approximate location of generalized hydrogeological cross section used to construct a numerical model used in the sensitivity study. (b) Comparison of simulated and observed uplift rates along A-A'. (c) Generalized hydrogeological cross section along A-A'. The cross section starts within the Canadian Shield before crossing the Michigan and Illinois Basins. The cross section terminates in the Gulf of Mexico coastal plain.

aquifer (illustrated in Figure 2a), which might likely have initiated groundwater upwelling that will eventually reach the surface (Christiansen et al., 1982). Blow out structures are then generated when fluid pressures exceed the weight of the overburden on the land surface (Christiansen et al., 1982). About 50 hydrodynamic blow out structures analogous to Howe Lake have been mapped in southeastern North Dakota (Bluemle, 1993). Carbon-14 dating of their sediments indicates that they formed at the onset of deglaciation.

Many prior hydrogeologic models of ice sheet loading have used vertical representations of ice sheet loading to drive groundwater flow within glaciated basins (e.g., Bense & Person, 2008; Lemieux et al., 2008a, 2008b, 2008c), while others have incorporated multidimensional stress fields in their analyses (e.g., Khader & Novakowski, 2014; Neuzil & Provost, 2014; Vinard et al., 1993, 2001). None, to date, have considered how failure might modify permeability conditions (e.g., Rojstaczer et al., 2008).

In this study, we assess temporal and spatial patterns of rock failure and associated permeability increases by analyzing the combination of stress state and pore pressure changes induced by ice sheet loading. We also consider how permeability increases impact solute transport in sedimentary basins over 10 glacial cycles. Our study is motivated, in part, because prior paleohydrologic reconstructions of Pleistocene glaciations of the midcontinent region of North America have had to use relatively high aquifer permeabilities ($\sim 10^{-11} \text{ m}^2$; e.g., McIntosh et al., 2011) in order to account for relatively deep glacial meltwater emplacement along the margins of sedimentary basins. Yet hydraulic testing of these same formations yields permeabilities that are 40 to 30,000 times lower (Gupta & Bair, 1997). This suggests that permeability may have evolved dynamically during the Pleistocene (Rojstaczer et al., 2008). We also assess how different representations of geomechanical stress state changes, induced by glacial loading, impact calculated anomalous fluid pressure conditions in confining units of sedimentary basins.

Due to the inherently large spatial and temporal scales of the problem, we have developed a multiphysics numerical model that partially couples a continental-scale (100 km by 2,800 km) lithosphere-asthenosphere geomechanical model with a basin-scale (7 km by 1,600 km) hydrological model. We use the mean normal stress change rates calculated by the geomechanical model and the failure region predicted by Coulomb Failure Stress change (ΔCFS_p) to drive the fluid flow and solute transport within two linked, idealized sedimentary basins that have undergone ten 100,000-year cycles of continental glaciations. The hydrogeological conditions are loosely based on the glaciated midcontinent region of North America (Figure 3). The crystalline basement is overlain by a confining unit in all but one scenario where we flipped the aquifer and confining unit ordering such that a basal aquifer directly overlays the crystalline basement.

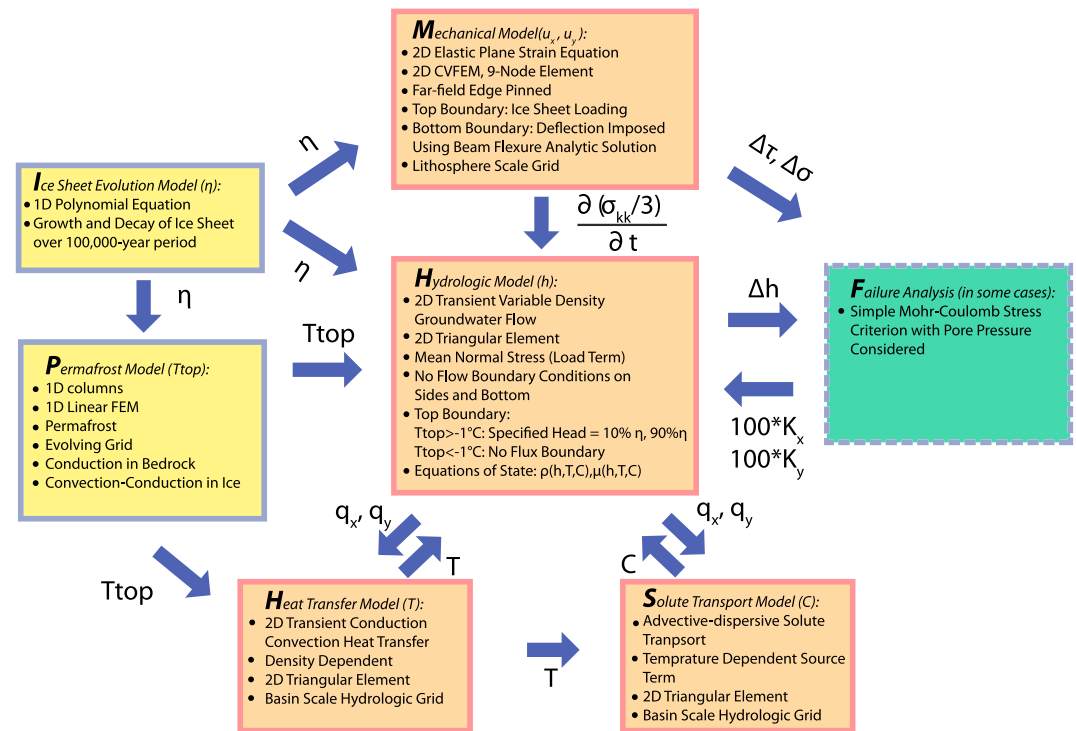


Figure 4. Schematic diagram depicting connections between different modules (geomechanical, hydrologic, heat transfer, and solute transport) represented in the multiphysics model used in this study. Variables include T_{top} (land surface temperature), $\frac{\partial}{\partial t} \left(\frac{\sigma_{kk}}{3} \right)$ (rate of mean normal stress changes), η (ice sheet thickness), q_x, q_y (Darcy flux), T (temperature), C (salinity), k_x and k_y (permeability), Δh (changes in hydraulic heads), and $\Delta\sigma, \Delta\tau$ (changes in normal and shear stresses). See supporting information for a more detailed discussion of transport processes represented.

2. Methodology

2.1. Processes Represented and Their Connections

The four primary components of our multiphysics code include mechanical, hydrologic, solute transport, and heat transfer modules (Figure 4). The mechanical module calculates displacement of an elastic lithosphere disturbed by an ice sheet load. Transient geomechanical deformation is represented by one-dimensional (lateral) viscous asthenosphere flow. Our geomechanical module is partially coupled to the hydrologic module by providing the rate of change in the mean normal stress $\left(\frac{\partial}{\partial t} \left(\frac{\sigma_{kk}}{3} \right) \right)$, $\sigma_{kk} = \sigma_{xx} + \sigma_{yy} + \sigma_{zz}$. Mean normal stress change rate is included as a source term in the groundwater flow equation driving flow (Neuzil, 2012). Skempton's coefficient was varied between 0.5 and 1. Flow is also influenced by changes in the top specified hydraulic head boundary condition (either 10% or 90% of ice sheet height). We neglected the effects of pore pressure changes on calculated displacements, which have been shown to result in small errors for cases with extensive vertical loading and small lateral strain (Gambolati et al., 2000; Ingebritsen et al., 2006; Neuzil, 2012). We implement two-way coupling among fluid flow, solute transport, and heat transfer module via density and viscosity equations of state. The governing equations and solution schemes used in our multiphysics code are described in the supporting information.

Three additional modules in our multiphysics code calculate changes to the upper hydraulic and thermal boundary conditions or alter the hydraulic transport properties (permeability) due to hydrogeomechanical failure. These include ice sheet evolution, permafrost, and failure analysis modules (Figure 4). Ice sheet thickness (η) determines both the vertical load in the geomechanical module and the hydraulic head boundary condition at the land surface in the hydrologic module (Figure 4). To represent waxing and waning of ice sheets through cyclical evolving ice sheet thickness (η) during glaciations and interglacial periods, prior hydrologic studies have used global geodynamic models (e.g., Neuzil & Provost, 2014; Tarasov & Peltier, 2007) or marine isotopic records (e.g., Cohen et al., 2010). In this study we adopted a simple parabolic

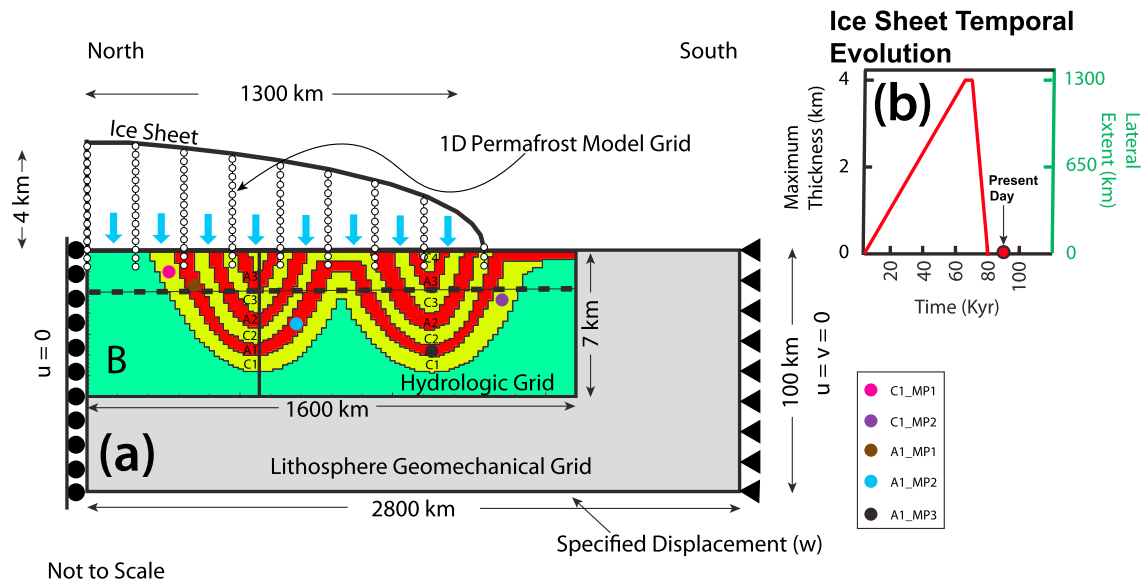


Figure 5. Schematic diagram depicting (a) the geomechanical and hydrologic model domains and hydrostratigraphic units (green crystalline basement; yellow shale confining units C1, C2, C3, and C4; and red aquifers A1, A2, and A3) for Scenarios #1–#8. (b) Idealized ice sheet history used in this study. One-dimensional finite element grids within the ice sheet and 750 m below the land surface used to compute permafrost evolution are shown in hollow dots. Blue arrows depict the specified load from the ice sheet imposed on the lithosphere. Three monitoring points in the basal aquifer (A1_MP1, brown; A1_MP2, blue; and A1_MP3, black) and two monitoring points in the basal confining unit (C1_MP1, pink, and C1_MP2, purple) are denoted by the colored dots.

polynomial equation to represent the idealized geometry of an ice sheet’s cross section (Van der Veen, 1999) in the ice sheet evolution module:

$$\eta(x, t) = H(t) \sqrt{1 - \left(\frac{x}{L(t)}\right)^2} \quad (1)$$

where $\eta(x, t)$ is the ice sheet thickness at location (x) and time (t), x is the distance from the location of maximum ice sheet thickness (the divide), $H(t)$ is the maximum ice sheet thickness at the divide at time t , and $L(t)$ is maximum lateral extent, or distance between the terminus and the divide, of the ice sheet at time t . The advance and retreat of the ice sheet through a glacial cycle was represented through changing the value of $H(t)$ and $L(t)$, both of which are linear functions of time (see Figure 5b). Our analysis neglects the short time scale (10,000 years) glacial retreats and readvances revealed in marine and ice sheet isotopic records (Imbrie et al., 1984; Johnsen et al., 1995).

Permafrost can prevent sub-ice sheet meltwater recharge (Kleinberg & Griffin, 2005; McKenzie et al., 2007). During the Pleistocene, permafrost formed across North America and Europe near the terminus of the ice sheets (Cutler et al., 2000; Péwé, 1983). However, thick (>1-km) ice cover has an insulating effect on the land surface and raises soil temperatures above the freezing point (Cutler et al., 2000). We solved for permafrost formation at and below the land surface using a suite of one-dimensional heat transfer models. We allowed for grid growth within the permafrost module (see the supporting information) to account for changes in ice sheet thickness. We only represented heat conduction below the land surface (upper 750 m) in these column models. We did represent both vertical convection and conduction within the ice sheet. The simulated temperatures at the land surface (T_{top}) were used to determine whether a no-flux ($T_{top} < 0$) or a specified head boundary ($T_{top} > 0$) is imposed in our hydrologic model. The land surface temperatures from these column models were also used as the upper specified temperature boundary condition in a two-dimensional basin-scale, two-dimensional, conductive-convective subsurface heat transfer model described in the supporting information.

A failure analysis module was used to modify permeability due to hydromechanical failure. We adopted the effective Coulomb’s Failure Stress change (ΔCFS_p) criterion from Ge et al. (2009) to assess regions of failure during glaciations:

$$\Delta CFS_p = \Delta\tau - \mu\Delta\sigma_n + \mu P \quad (2)$$

where ΔCFS_p is the effective Coulomb Failure Stress change, $\Delta\tau$ and $\Delta\sigma_n$ are, respectively, glacial loading induced changes of shear stress and normal stress on critically stressed fault planes, μ is the friction coefficient, and ΔP is the change of pore pressure on the fault plane due to, both, glacial loading induced volumetric change (undrained response) and subglacial meltwater-induced pressure diffusion. A positive value of ΔCFS_p suggests the possibility of instability along a critically stressed fault and thus a higher likelihood of failure (Ge et al., 2009). Previous studies have argued that relatively small effective Coulomb Failure Stress increase ($> = 0.01$ MPa) can result in increased seismicity (Stein, 1999) and hasten the nucleation of a large earthquake by tens of hundreds of years (Ge et al., 2009). Roeloffs (1988, 1996) indicated a critical threshold of 0.1 MPa for surface water reservoir-induced (i.e., loading related) seismicity. Similarly, King et al. (1994), Stein (1999), and Stein et al. (1992, 1994) suggested that small static stress change of 0.1 MPa (equivalent to 10 m of head) and less can probably trigger seismicity. In this study, we used the more conservative value of 0.1 MPa as failure threshold. Once the simulated Coulomb Failure Stress change (ΔCFS_p) exceeds this threshold, we multiply the permeability (k_x, k_y) within the failure region by 100. We further assume that critically stressed faults with orientations of 30° from the maximum principal stress (σ_1) are widely distributed in the upper lithosphere, which has been supported by the seismic profiles of deep faults beneath the Illinois basin near the New Madrid seismic zone (McBride et al., 2007). Using thermal anomaly data in wells, Townend and Zoback (2000) found that there are numerous critically stressed faults in the borehole they analyzed, and they implied that the widely distributed critically stressed faults are key to keeping the continental crust in a failure equilibrium state. In some simulations, we focused on purely geomechanical effects on failure by applying a Coulomb Failure Stress change criterion without a pore pressure term:

$$\Delta CFS = \Delta\tau - \mu\Delta\sigma_n \quad (3)$$

2.2. Numerical Methods and Model Domain

The numerical model used in this study is implemented on a 2-D cross-sectional Cartesian coordinate system (Figure 5). Many prior studies modeling the subsurface stress changes due to ice sheet loading (e.g., Johnston et al., 1998; Klemann & Wolf, 1998) used a cylindrical coordinate system due to the approximate radial symmetry of continental ice sheets. However, our primary focus was on groundwater flow and solute transport in sedimentary basins where a Cartesian coordinate made the most sense for this purpose.

2.2.1. Geomechanical Model

We solved a 2-D plane strain elasticity equation (equation (S1) in the supporting information; Ge & Garven, 1992; Voller, 2009) to represent lithosphere deformation in our geomechanical model. The model domain is a 2,800 km long by 100-km-thick rectangle (Figure 5a) discretized into 3,091 nine-node rectangular control volume finite elements (Voller, 2009; 281 nodal columns and 11 nodal rows with $\Delta x = \Delta y = 10$ km). We found that lower order elements (e.g., triangle elements) resulted in shear locking (Bletzinger et al., 2000) and thus used nine-node elements to resolve this issue. The southern (right) side boundary, located 1,500 km south of the ice sheet terminus, was assigned a zero-displacement condition in both x and y directions. We allowed for vertical (y direction) displacements along the northern (left) boundary. No horizontal displacements were permitted at the left boundary, as they are zero under the center of a radially symmetric load (e.g., Grapenthin, 2014). Along the top boundary of the domain, we specified a stress boundary determined by the weight of the ice sheet at grid locations:

$$P_{ice}(x, t) = \rho_{ice}g\eta(x, t) \quad (4)$$

where $P_{ice}(x, t)$ is the weight of the ice sheet, ρ_{ice} is the ice density, g is gravitational acceleration, and $\eta(x, t)$ is the ice sheet thickness varying in space and time through glacial cycles. Along the bottom boundary we specified displacements using analytical solutions to a beam bending equation (Turcotte & Schubert, 2001; Van der Veen, 1999; see equations (S5)–(S7) in the supporting information) to account for viscous flow of the asthenosphere. The geomechanical model was solved using a time step size of 1,000 years. We evaluated our geomechanical model, in part, by comparing modeled displacements for a test problem to results from the commercial package ANSYS®.

2.2.2. Hydrologic, Solute, and Heat Transport Model

Our analysis considers groundwater flow driven by elevated hydraulic heads beneath the ice sheet (e.g., Person et al., 2007), the rate of mean normal stress change associated with mechanical loading of the ice

sheet (e.g., Neuzil & Provost, 2014), and variable-density effects induced primarily by salinity variations within the crystalline basement (e.g., Lemieux et al., 2008a; Park et al., 2009) and overlying sedimentary basin (e.g., McIntosh et al., 2011). The governing equation we solved for groundwater flow is similar to the one presented by Neuzil and Provost (2014) but in two spatial dimensions:

$$\frac{\partial}{\partial x} \left[\frac{\rho_0 g}{\mu_f} \left(k_x \frac{\partial h}{\partial x} \right) \right] + \frac{\partial}{\partial y} \left[\frac{\rho_0 g}{\mu_f} \left(k_y \frac{\partial h}{\partial y} \right) \right] = S_s \frac{\partial h}{\partial t} - \rho_r k_y \frac{\rho_0 g}{\mu_f} - \frac{S_s B}{\rho_f g} \frac{\partial}{\partial t} \left(\frac{\sigma_{kk}}{3} \right) \quad (5)$$

where k_x and k_y are the components of the permeability in the x and y directions, h is hydraulic head, t is time, g is gravitational acceleration, μ_f is fluid viscosity, ρ_0 is reference fluid density ($1,000 \text{ kg/m}^3$), ρ_f is fluid density, ρ_r is relative density [$\rho_r = (\rho_f - \rho_0)/\rho_0$], and S_s is specific storage. Fluid density and viscosity were computed in this study using the equations of state presented in Batzle and Wang (1992). σ_{kk} is the total normal stress ($\sigma_{kk} = \sigma_{xx} + \sigma_{yy} + \sigma_{zz}$). B is Skempton's coefficient or loading efficiency. The Skempton's coefficient is defined as the proportion of external load supported by the pore fluid, and generally, it varies from 0.5 to close to 1 depending on the mechanical properties of the fractured or porous medium. Variable-density flow effects were incorporated in our model because groundwater in most sedimentary basins across North America has total dissolved solid concentrations varying from fresh at shallow depths ($\sim 100 \text{ m}$) to in-excess-of-sea-water-salinity at deeper depths (up to 5 km ; McIntosh et al., 2011). The last term on the right-hand side of equation (5) represents the rate of change of the mean normal stress determined from the geomechanical model and is equivalent to a fluid source or sink term distributed at each node (Neuzil, 2012). Like prior studies by Lemieux et al. (2008a) and Neuzil and Provost (2014), the groundwater flow equation we solved in our model was not coupled to the geomechanical model for reasons mentioned in section 2.1. We used an interpolation algorithm to impose the rate of the change in mean normal stress, $\frac{\partial}{\partial t} \left(\frac{\sigma_{kk}}{3} \right)$, on to our hydrologic model domain in order to calculate changes in pore pressures and salinity in response to ice sheet loading.

The hydrologic, solute, and heat model were solved on a $1,600\text{-km}$ wide by 7-km -thick rectangular domain (Figure 5a). Our hydrologic model was thinner than the geomechanical model because it is generally assumed that a free liquid phase connected to the land surface only exists in the upper $10\text{--}12 \text{ km}$ (Zoback & Townend, 2001). We used a more refined grid of 101 nodal columns and 71 nodal rows ($\Delta x = 1,600 \text{ m}$, $\Delta y = 100 \text{ m}$; 7,171 nodes). The geomechanical failure analysis variables (ΔCFS in equation (3)) computed in the lithosphere-scale model were interpolated onto the hydrologic grid. We used a traditional triangular finite element discretization that employed a linear trial solution to solve the 2-D groundwater flow and heat transport equations. The modified method of characteristics was used to solve the solute transport equation (see the supporting information).

The hydrologic model extended 300 km beyond the southern margin of the ice sheet (Figure 5a). We used idealized stratigraphic layers in the model. Three major hydrostratigraphic units (basement, aquifers, and confining units) were included in the model (Figure 5a). We included up to four aquifers labeled as A1 to A4 and up to four confining units labeled as C1 to C4. We included two sedimentary basins that are adjacent to each other in our model. This is loosely based on the geology of the Michigan Basin and Illinois Basin. The sedimentary basin units are underlain by crystalline basement rocks labeled as B in Figure 5a. In most simulations, a basal confining unit overlaid the crystalline basement (Scenarios # 1–8). We considered one scenario (#9), in which a basal aquifer overlaid the crystalline basement. The hydrologic model was solved using a time step size of 100 years. We monitored heads and salinity at three points in the basal aquifer (A1_MP1, A1_MP2, and A1_MP3 in Figure 5a); we also monitored heads along a vertical profile ($x = 560 \text{ km}$; a solid line) and salinity along a lateral profile ($y = 1,500 \text{ m}$; a dashed line).

Many prior hydrogeologic studies that focused on brine flushing assigned a specified upper head boundary condition at the land surface that is consistent with ice sheet *floating conditions* (fluid pressures that support the entire weight of the ice sheet is equivalent to 90% of ice sheet thickness; e.g., Cohen et al., 2010; McIntosh et al., 2011; Person et al., 2003). Most studies that focused on reproducing observed anomalous underpressures in tight confining units have assigned heads equal to 10% of ice sheet thickness along the top boundary (e.g., Khader & Novakowski, 2014). Using this boundary condition renders the geomechanical source/sink term in the groundwater flow equation greater influence (Neuzil & Provost, 2014). As described above, for the hydrologic top boundary condition we assigned a no-flux boundary to a nodal column if the land surface temperature (T_{top} in Figure 4) was less than zero. If the land surface temperature was above zero,

Table 1
Properties Used in the Model for Lithosphere and Asthenosphere

| Property name | Value |
|---|--|
| Young's modulus of lithosphere (E) | 56 GPa/192 GPa |
| Poisson ratio (ν) | 0.25/0.4 |
| Elastic thickness of lithosphere (L) | 100 km |
| Flexural rigidity of lithosphere ($D \equiv \frac{EL^3}{12(1-\nu)}$) | $6.22 \times 10^{24}/26.67 \times 10^{24} \text{ Pa}\cdot\text{m}^3$ |
| Diffusivity of asthenosphere ($D_a \equiv \frac{qH^2}{3\eta}$) | 50 km ² /yr |
| Mantle density (ρ_m) | 3,380 kg/m ³ |
| Ice density (ρ_{ice}) | 900 kg/m ³ |
| Gravitational constant (g) | 9.812 m/s ² |

we used a specified head boundary condition of either 10% or 90% of the ice sheet elevation in different simulation scenarios:

$$\begin{aligned} h_{bc}(x, t) &= 0.1\eta(x, t) \\ h_{bc}(x, t) &= 0.9\eta(x, t) \end{aligned} \quad (6)$$

where $h_{bc}(x, t)$ is the specified head and $\eta(x, t)$ is the ice sheet thickness. If no ice was present, the land surface elevation was specified. We hypothesize that sedimentary aquifers overlain by till deposits are not exposed to fluid pressures as high as 90% of ice sheet thickness. Thus, in most of the simulations presented below we used 10% of the ice sheet height as an upper hydraulic head boundary condition. No flux boundaries were assigned to the bottom and sides of the hydrologic model solution domain. Hydrostatic heads were assigned as an initial condition. We veri-

fied the hydrologic model, in part, using the analytical solutions from Lemieux et al. (2008b) and Walsh et al. (2012; see the supporting information).

To assess the effects of ice sheet loading on brine migration and temperature distribution within sedimentary basins, we solved the advection-dispersive solute transport equation and the convection-conduction heat transfer equation (see the supporting information for details).

In the solute transport model, all domain boundaries except the top are no-flux boundaries. The top boundary is a specified value boundary with zero salinity assigned. We imposed a linear increase of salinity with depth as an initial condition for solute transport. At the base of the domain, the initial salinity was 42 ppt. Our idealized analysis of Pleistocene hydrogeologic conditions neglects the underlying mechanisms of brine formation that, for the midcontinent region of North America, have been linked to evaporite dissolution and evapoconcentration of seawater during Paleozoic and Mesozoic Eras (Hanor, 1979; Hanor & McIntosh, 2006). However, we included a salinity source term in the crystalline basement nodes as described by Lemieux et al. (2008b).

In the heat transfer model, we used the land surface temperature (T_{top}) computed from the permafrost model to assign the temperatures along the top of the boundary, and we assumed insulated side boundaries ($dT/dz = 0$) and a basal heat flux condition of 60 mW/m². The initial condition was set to be a linear geothermal gradient of 26 °C/km.

2.2.3. Permafrost Model

Permafrost evolution was evaluated using a series of independent vertical columns that consist of one-dimensional linear finite elements. The nodes, represented by the hollow dots inside the ice sheet in Figure 5a, have a spacing of 10 m. Within the permafrost model, we allowed the solution domain to grow dynamically along each nodal column as ice sheet thickness changed (i.e., the number of nodes changed in each local 1-D column of the permafrost model). Unglaciated areas always had 76 nodes and 75 elements. And at the ice sheet divide during each glacial maximum, 476 nodes were used when the ice sheet reached its maximum thickness at 4,000 m. The permafrost model was solved using a time step size of 1 year due to the nonlinear effects of permafrost formation.

A more detailed discussion of the methodology can be found in the supporting information (Cohen et al., 2018; Ellis & Mahon, 1964, 1967; Kim et al., 2008; Konikow & Grove, 1977; Scheidegger, 1961; Timoshenko & Goodier, 1970; Walcott, 1970; Wang & Anderson, 1982; Zheng & Bennett, 1995).

2.3. Simulation Scenarios and Model Parameters

We developed transient hydrologic and geomechanical models (Figure 5a) of the late Pleistocene (last million years) using ten 100-Kyr glacial cycles (Figure 5b). This represents an approximation of the ice sheet reconstruction from Marshall et al. (2002). Each glacial cycle consisted of 69 Kyrs of ice sheet growth (0–69 Kyr) and 10 Kyrs of retreat (70–80 Kyr) followed by a 20-Kyr interglacial period (ice free conditions). Maximum ice sheet height persisted for only 1,000 years between 69 and 70 Kyr. We will refer to this time period as the LGM (Last Glacial Maximum). We will refer to EoG (End of Glaciation) as the time when the ice sheet thickness disappeared (80 Kyr into the ice sheet cycle) and MOD as the present-day (90 Kyr into the ice sheet cycle). The 20-Kyr ice-free time in the ice sheet history can be observed in the period from 120 BP to 100 BP from Marshall et al. (2002).

Table 2
Parameter Sensitivity Study Summary

| Sim. No. | Rheology | ^a Loading scheme | ^b Permeability | Skempton constant | ^c Top hydro. boundary | ^d Hydrostat. order | Figure |
|----------|--------------------------------|-----------------------------|---------------------------|-------------------|----------------------------------|-------------------------------|---------------|
| 1 | ^e Grollimund-Zoback | 3-D | Static | 1 | 0.1 | Norm | 8 and 10–13 |
| 2 | Grollimund-Zoback | 3-D | Dynamic | 1 | 0.1 | Norm | 10–12 |
| 3 | ^f Lund-Wu | 3-D | Static | 1 | 0.1 | Norm | 8, 10, and 11 |
| 4 | Lund-Wu | 3-D | Dynamic | 1 | 0.1 | Norm | 10–12 |
| 5 | Grollimund-Zoback | 1-D vertical | Static | 1 | 0.1 | Norm | 8, 10, and 11 |
| 6 | Grollimund-Zoback | 3-D | Static | 1 | 0.9 | Norm | 9–12 |
| 7 | Grollimund-Zoback | 3-D | Dynamic | 1 | 0.9 | Norm | 10–12 |
| 8 | Grollimund-Zoback | 3-D | Static | 0.5 | 0.1 | Norm | 9 |
| 9 | Grollimund-Zoback | 3-D | Static | 1 | 0.1 | Reverse | 9 and 13 |

^aThe 1-D = $(\frac{\partial \sigma_{yy}}{\partial t})$ or 3D = $(\frac{\partial}{\partial t} (\frac{\sigma_{kk}}{3}))$. ^bDynamic, permeability increase by 100-fold in aquifers if $\Delta CFS_p > 0.1$ MPa; Static permeability, permeability remains constant for all values of ΔCFS_p . ^c0.1, 0.9, impose 10% or 90% of ice sheet thickness respectively. ^dNorm aquifer/confining unit order is consistent with Figure 5a and reverse, basal aquifer directly overlies the crystalline basement. ^e $E = 56$ GPa, $\nu = 0.25$. ^f $E = 192$ GPa, $\nu = 0.4$.

We ran dozens of simulations varying Young’s modulus and Poisson’s ratio for the homogeneous isotropic lithosphere (Table 1); we also varied the permeability with a wide range of values for the three different hydrostratigraphic units (10^{-11} to 10^{-15} m², for aquifers; 10^{-18} to 10^{-21} m², for confining units; and 10^{-14} to 10^{-18} m² for the crystalline basement) as part of a preliminary sensitivity study. Because the focus of this analysis is on hydromechanical failure and its effects on permeability changes, we present only nine scenarios here (Table 2). The aquifer and confining unit permeability values presented represent intermediate range of observed conditions (Gupta & Bair, 1997; Neuzil, 1994; Freeze & Cherry, 1979). The permeability anisotropy (k_x/k_y ; Table 3) for both the aquifers and confining units was set at 10. We assume that the basement has isotropic with a constant permeability of 10^{-16} m², which is consistent with the values reported by Ingebritsen and Manning (2010), Stober and Bucher (2007), and Townend and Zoback (2000).

The vertical confining unit permeability we used is 10^{-20} m² (Table 3), which is about 1 order of magnitude lower than average value for shales reported by Neuzil (1994) and 1 order of magnitude higher than the best fit assigned to tight argillaceous units at the Bruce site within the Michigan Basin by Neuzil and Provost (2014). Without such tight permeability conditions, modern underpressures were not preserved in our model. The other hydrogeologic properties assigned to solve the groundwater flow equation are listed in Table 3. Additional properties used to solve the heat and solute transport equations are listed in Table 4. These are typical values for porous media and fractured crystalline rocks (Smith & Chapman, 1983).

2.3.1. Rheology

For most simulations listed in Table 2, we used a Young’s modulus of 56 GPa and a Poisson’s ratio of 0.25 (Table 1). These values were taken from Grollimund and Zoback (2000). These authors assessed the effects of glaciation on stress fields within the North Sea. We refer to these simulations as *Grollimund-Zoback* scenario under the rheology column in Table 2. Lund (2005) and Wu (1992), on the other hand, used a Young’s modulus of 192 GPa and a Poisson’s ratio of 0.5 in order to represent glacial isostatic adjustment-affected stresses, displacements, and fault stability during deglaciation in northern Scandinavia. We ran several simulations using a Young’s modulus of 192 GPa and a Poisson’s ratio of 0.4. We refer to these simulations as *Lund-Wu* Scenarios under the rheology column in Table 2.

2.3.2. Loading Scheme

Many prior studies (e.g., Lemieux et al., 2008a, 2008b, 2008c; Person et al., 2007) used temporal changes in the vertical load ($\frac{\partial \sigma_{yy}}{\partial t}$) rather than the mean normal stress [$\frac{\partial}{\partial t} (\frac{\sigma_{kk}}{3})$] to represent anomalous pressure generation due to glaciation. We explore the ramifications of using the one-dimensional vertical loading in Scenario #5. One drawback is that the ΔCFS_p failure criterion cannot be calculated.

2.3.3. Dynamic Versus Static Permeability

In some simulations, we allowed elemental permeability to increase by 100-fold in aquifers, confining units, and basement (Rojstaczer et al., 2008) whenever the nodal hydromechanical failure criteria (ΔCFS_p)

Table 3
Hydrogeologic Properties Used in Model

| Property name | Value |
|---|---------------------------|
| Specific Storage (S_s)* | 10^{-6} m ⁻¹ |
| Bedrock permeability ($k_x = k_y$; m ²) | 10^{-16} m ² |
| Skempton constant (B) | 0.5, 1 |
| Aquifer permeability (k_x, k_y ; m ²) | 10^{-14} , 10^{-15} |
| Confining unit permeability (k_x, k_y ; m ²) | 10^{-19} , 10^{-20} |

Note. Asterisk denotes applied to all units.

Table 4
Transport Properties Used in the Heat and Solute Mass Transfer Equations

| Property name | Value |
|---|--------------------------|
| Solid thermal conductivity (λ_s) | 2.5 W · m · °C |
| Fluid thermal conductivity (λ_f) | 0.58 W · m · °C |
| Longitudinal dispersivity (α_L) | 100 m |
| Transverse dispersivity (α_T) | 10 m |
| Fluid specific heat capacity (c_f) | 1,000 J/kg |
| Solid specific heat capacity c_s | 1,000 J/kg |
| Fluid density (ρ_f) | 1,000 kg/m ³ |
| Solid density (ρ_s) | 2,650 kg/m ³ |
| Solute diffusivity (D_s) | 0.035 m ² /yr |
| Porosity of crystalline basement, sandstone, and shale (ϕ) | 0.05, 0.2, 0.3 |
| Rock – water interaction constant (A_o) | 0.002 t ⁻¹ |
| Activation Energy (E_o) | 8,314 J · mol · °C |
| Universal gas constant (R) | 8.314 J/mol |
| Maximum concentration (C_{max}) | 0.06 mass fraction |

exceeded a threshold value of 0.1 MPa (equivalent to 10 m of head). If the failure criteria subsequently fell below this threshold, permeability was instantaneously returned to its initial value. Since our hydrogeologic time step size is 100 years, this assumption seems reasonable. We refer to these scenarios as *dynamic* case. In some simulations, permeability was held constant. We refer to these scenarios as *static* cases (Table 2). Scenarios #2 and #7 are Dynamic cases using the Grollmund-Zoback rheology, and Scenario #4 is a Dynamic case using the Lund-Wu rheology.

2.3.4. Skempton's Coefficient

Skempton's coefficient determines how much of the mechanical load is supported by the fluid phase versus the rock phase. A Skempton's coefficient of 1 means that an imposed load can be fully supported by the fluid phase—for an impermeable medium, the fluid pressure will equal the weight of the imposed load. When Skempton's coefficient is zero, none of the load is supported by the fluid phase. Measurements of Skempton's coefficient suggest that the range for sandstone, shale, and carbonate are 0.58–1.0, 0.98–0.99, and 0.73–1.0, respectively (data source:

Green & Wang, 1986; Haas et al., 1989; Neuzil, 1993). In all but one simulation, we used a Skempton's coefficient of 1 for both sediment and basement. In Scenario #8, we used 0.5.

2.3.5. Upper Hydrologic Boundary Condition

In most scenarios presented in this study, we imposed a specified head top boundary condition equal to 10% of ice sheet thickness. However, in Scenarios #6 and #7 we imposed a specified head equal to 90% of ice sheet thickness as the top boundary condition.

2.3.6. Hydrostratigraphy Order

For most cases listed in Table 2, the hydrostratigraphy order is consistent with the one shown in Figure 5a. In one scenario (Scenario #9, Table 2) we explored the sensitivity of stratigraphic order on the computed heads and hydromechanical failure. In this scenario, we flipped over the stratigraphy order so that a basal aquifer directly overlies the crystalline basement. In Scenario #9, the four aquifers are labeled as A1–A4, and the three confining units are labeled as C1–C3.

3. Results

3.1. Glacially Induced Changes in Normal Stress Fields

We begin by presenting calculated glacial induced normal stress changes ($\hat{\sigma}_{xx}$, $\hat{\sigma}_{yy}$, $\hat{\sigma}_{zz}$; where the caret (^) denotes the stress changes with respect to the ice free stress state) using Grollmund-Zoback rheology at four different times during glacial advance and retreat within one glacial cycle (Figure 6). The stress changes computed using the Lund-Wu rheology are presented in the supporting information (section S4.1).

Figure 6 presents the changes in the stress fields due to glacial loading in a portion (2,300 km by 100 km) of the solution domain proximal to the ice sheet. The red circles in the left column of Figure 6 indicate the current ice sheet thickness of the ice sheet in each row. The lateral extent of the ice sheet is schematically represented by the solid black rectangle at the top of the contour plots in Figure 6. The approximate parabolic geometry of the ice sheet is illustrated in Figure 5a. The dashed rectangle denotes the boundary of the refined hydrologic grid.

As the ice sheet begins to grow and extends southward (to the right), the vertical normal stress changes ($\hat{\sigma}_{yy}$) increases (Figures 6i–6j) but do not vary much with depth. The magnitude of the normal stress equals the ice sheet weight (i.e., the vertical load) imposed on each point of the top boundary. At LGM (Figure 6j), the ice sheet reached its maximum thickness (4,000 m at $x = 0$ km) and the corresponding maximum increase in the vertical normal stress $\hat{\sigma}_{yy}$ was 35.3 MPa. From EoG to MOD (Figures 6k–6l) the vertical normal stress changes are zero everywhere.

Horizontal normal or flexural stress changes ($\hat{\sigma}_{xx}$) are spatially more complex throughout the glacial cycle. As the ice sheet grows, we observe compressional stresses (positive values denoted by red/orange colors; Figures 6a and 6b) underneath the ice sheet, while dilatational stresses (negative values denoted by blue; Figures 6a and 6b) occur beyond the terminus of the ice sheet in the upper 50 km of the lithosphere. Below 50-km deep, the flexural stress change patterns are inverted as expected given the applied beam

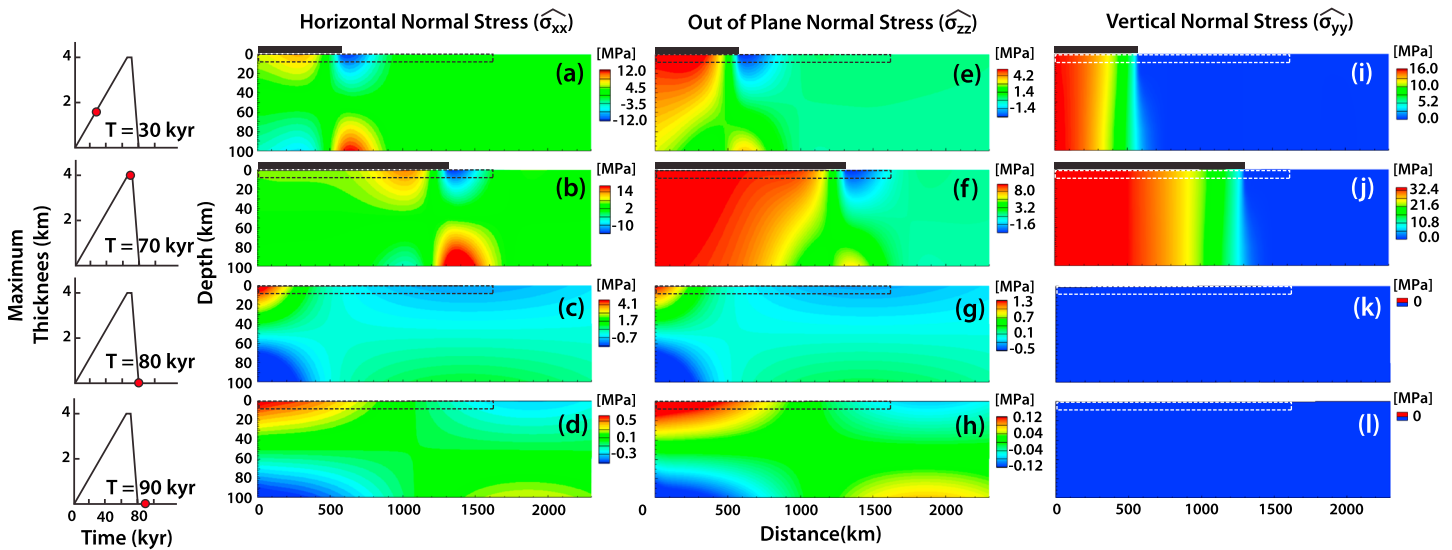


Figure 6. Computed changes in horizontal normal or flexural stresses due to glacial loading (left column, a–d), changes in out of plane normal stresses (middle column, e–h), and changes in vertical normal stresses (right column, i–l) in unit of MPa for the Grollmund-Zoback rheology at four different times within one glacial cycle: $T = 30$, $T = 70$ (LGM), $T = 80$ (EoG), and $T = 90$ Kyr (MOD). Black rectangles on the top of the model domain (a and b, e and f, and i–j) denote the lateral extension of the ice sheet. The dashed rectangle denotes the boundary of the refined hydrological grid. The red dots on the ice sheet evolution function on the left edge denote the time period at which the corresponding snapshot is taken. Note that each contour plot uses a different color scale.

bending theory. At LGM (Figure 6b), the highest compressive flexural stress increase (17 MPa) of the upper 50 km of the lithosphere appears near the land surface underneath the ice sheet, about 150 km to the north of the ice sheet terminus. This is the region least likely to mechanically fail. The maximum compressive stress is about one half of the maximum vertical normal stress change ($\hat{\sigma}_{yy} = 35.3$ MPa). Out in front of the ice sheet, dialational stress changes reach a minimum value of -16 MPa. This region is most likely to experience a shear failure due to ice sheet loading. Once the ice sheet is absent at EoG (Figure 6c), flexural stress changes drop in magnitude to about 20% of the LGM levels. The flexural stress changes are nonzero at EoG and MOD (Figures 6c and 6d), because the lithosphere has not returned to its underformed state. Viscous asthenospheric flow is relatively slow when compared to the rate of climatically induced glacial retreat. Flexural stresses continue to decline following EoG but are still nonzero at MOD. At MOD, the maximum compressive flexural stress increase is only 0.68 MPa and located slightly below the land surface near the origin (Figure 6d). Dialational flexural stress increases of interest up to -0.3 MPa appears near the southern (right) edge of the hydrologic grid (dashed rectangle).

The patterns of changes in out of plane normal stress ($\hat{\sigma}_{zz}$) represent averages of the $\hat{\sigma}_{xx}$ and $\hat{\sigma}_{yy}$ components, while the ice sheet is present (Figures 6e and 6f). The compressive (positive contour value) components of $\hat{\sigma}_{zz}$ extend to the bottom of the lithosphere, and the tensile (negative contour value) components only appear beyond the terminus of the ice sheet in the upper 50 km, which is similar to the out of plane incremental stress patterns caused by an ice load with a radius of 1,000 km that Johnston et al. (1998) modeled in a cylindrical coordinate system. The absolute values of $\hat{\sigma}_{zz}$ are about 50% less than $\hat{\sigma}_{xx}$ during the period when ice sheet is present (compare Figures 6e and 6f to Figures 6a and 6b). Once the ice sheet is completely gone, the spatial pattern of $\hat{\sigma}_{zz}$ resembles that of $\hat{\sigma}_{xx}$ but the magnitudes are about 75% smaller (compare Figures 6g and 6h to Figures 6c and 6d).

3.2. Temporal Changes in 3-D and 1-D Loading Source Terms

The mean normal stress change rates (MNSCR, $\frac{\partial}{\partial t} \left(\frac{\sigma_{kk}}{3} \right)$) are the source term producing the anomalous pressures in the groundwater flow equation (equation (5)), which was applied in Scenarios #1–#4 and #6–#9 (Table 2). Positive values of MNSCR generate overpressures (heads above hydrostatic conditions), while negative values of MNSCR will lead to underpressure formation (head below hydrostatic conditions). Figures 7a–7e present MNSCR over one glacial cycle using the Grollmund-Zoback rheology; Figures 7f–7j

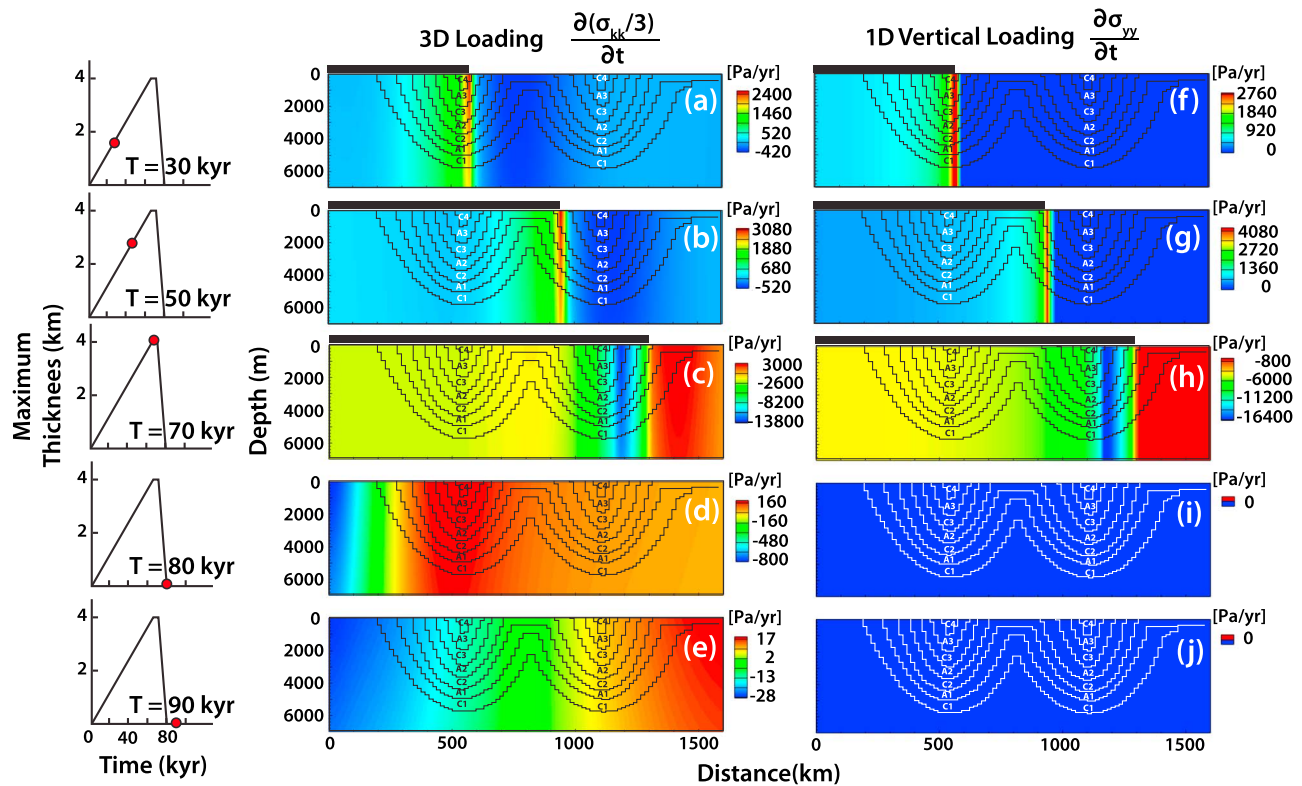


Figure 7. Ice sheet loading source terms used in groundwater flow equation during one glacial cycle in unit of Pa/yr for both the 3-D loading (left column, a–e; $\frac{\partial(\sigma_{kk}/3)}{\partial t}$) and 1-D vertical loading (right column, f–j; $\frac{\partial\sigma_{yy}}{\partial t}$). Both columns of the contour plots used the Grollmund-Zoback rheology. Black rectangles on the top of the model domain (a–c and f–h) denote the lateral extension of the ice sheet. The red dots on the ice sheet evolution function on the left edge denote the time period at which the corresponding snapshot is taken. Note that each contour plot uses a different color scale.

present a different source term distribution in the groundwater flow equation using the vertical loading change rate that is applied in Scenario #5.

During ice sheet advance the magnitudes of the three-dimensional loading (3-D) rates are about 15–25% lower than the one-dimensional (1-D) loading rates (compare Figures 7a and 7b to Figures 7f and 7g). Beyond the terminus of the ice sheet, the 1-D loading rates are zero, while the 3-D loading rates are negative as expected from results in section 3.1. At $T = 50$ Kyr, a maximum value of 3,100 Pa/yr is observed for the 3-D loading source term (Figure 7b), while the maximum 1-D value is 4,120 Pa/yr (Figure 7g). During ice sheet growth, the most negative 3-D value occurs beyond the ice sheet terminus and its value becomes more negative as simulation time approaches LGM (Figures 7a and 7b). The minimum value of -530 Pa/yr is observed at $T = 50$ Kyr for the 3-D loading source term (Figure 7b). In contrast, beyond the ice sheet terminus, the 1-D loading source term is always zero (Figures 7f and 7g) during ice sheet growth.

At the end of LGM, right before the ice sheet began to retreat, we observe a broad spatial change in the sign of both the 3-D and 1-D loading source terms: the values become positive beyond the ice sheet terminus and negative underneath the ice sheet. The absolute values during the ice sheet retreat are much larger (14,000 and 16,800 pa/yr for 3-D and 1-D, respectively) than during the ice sheet advance. This is because ice sheet retreats at a much faster rate over 10 Kyr than ice sheet advances over 69 Kyr. Once the ice sheet is removed at EoG and till MOD, the absolute values of 3-D are smaller but still nonzero (Figures 7d and 7e), while the 1-D values are zero (Figures 7i and 7j). The nonzero values result from the changes of the remnant $\hat{\sigma}_{xx}$ and $\hat{\sigma}_{zz}$ due to postglacial lithosphere rebound caused by viscous mantle flow underneath the lithosphere.

3.3. Permafrost Distribution

During ice sheet advance, permafrost developed—and imposed a hydrologic no flux boundary—beneath and up to about 250 km beyond the terminus of the ice sheet (see Figure S8 in the supporting

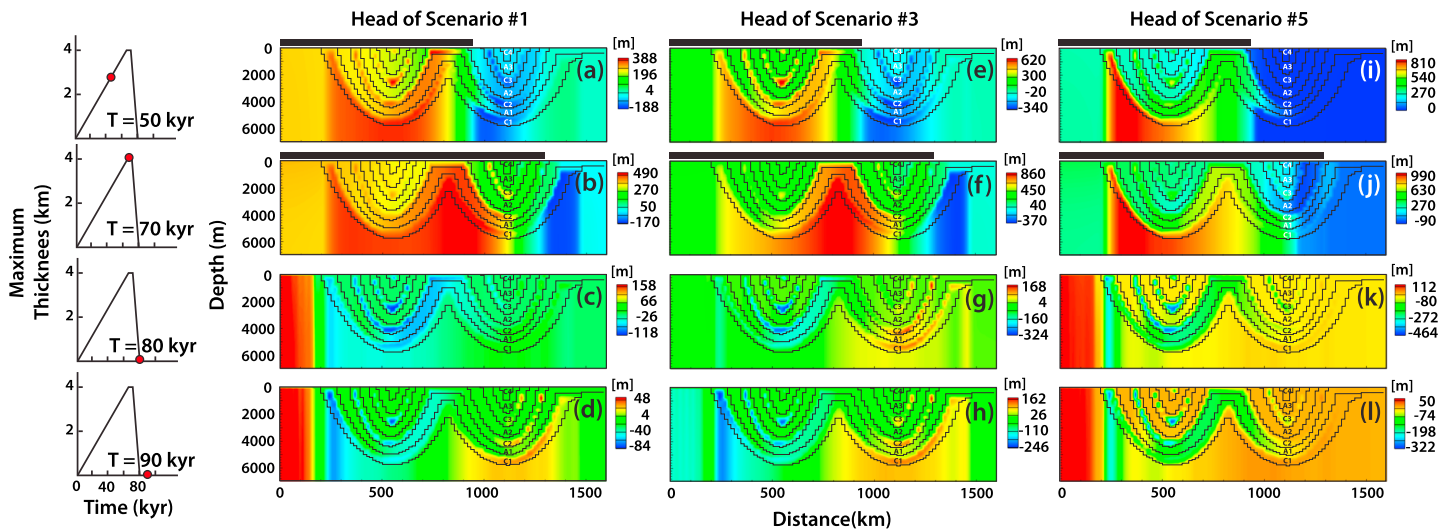


Figure 8. Computed heads of Scenario #1 (a–d), Scenario #3 (e–h), and Scenario #5 (i–l) after one glacial cycle. Black rectangles on the top of the model domain (a and b, e and f, and i–j) denote the lateral extension of the ice sheet. The red dots on the ice sheet evolution function on the left edge denote the time period at which the corresponding snapshot is taken. Note that each contour plot uses a different color scale. See Table 2 and text for detailed descriptions of different simulation scenarios.

information). Permafrost was absent in regions behind the ice sheet terminus where ice thickness exceeded 1,000 m but developed in the highest latitudes during interglacial periods. A more extensive discussion of permafrost dynamics can be found in section S4.2 of the supporting information.

3.4. Simulated Hydraulic Heads

In Figures 8 and 9 we compare and contrast simulated hydraulic heads during the first glacial cycle between 50,000 and 90,000 years into the simulation. Figure 8 shows results for Scenario #1 (Grollmund-Zoback rheology; Figures 8a–8d), #3 (Lund-Wu rheology; Figures 8e–8h), and #5 (vertical loading; Figures 8i–8l). These scenarios assume an upper hydrologic head boundary condition 10% of ice sheet thickness, static permeability, and a Skempton's coefficient of 1 (Table 2). Figure 9 presents additional head distribution for scenarios with a floating condition as the upper hydrologic boundary conditions (Scenario #6; Figures 9a–9d), reducing

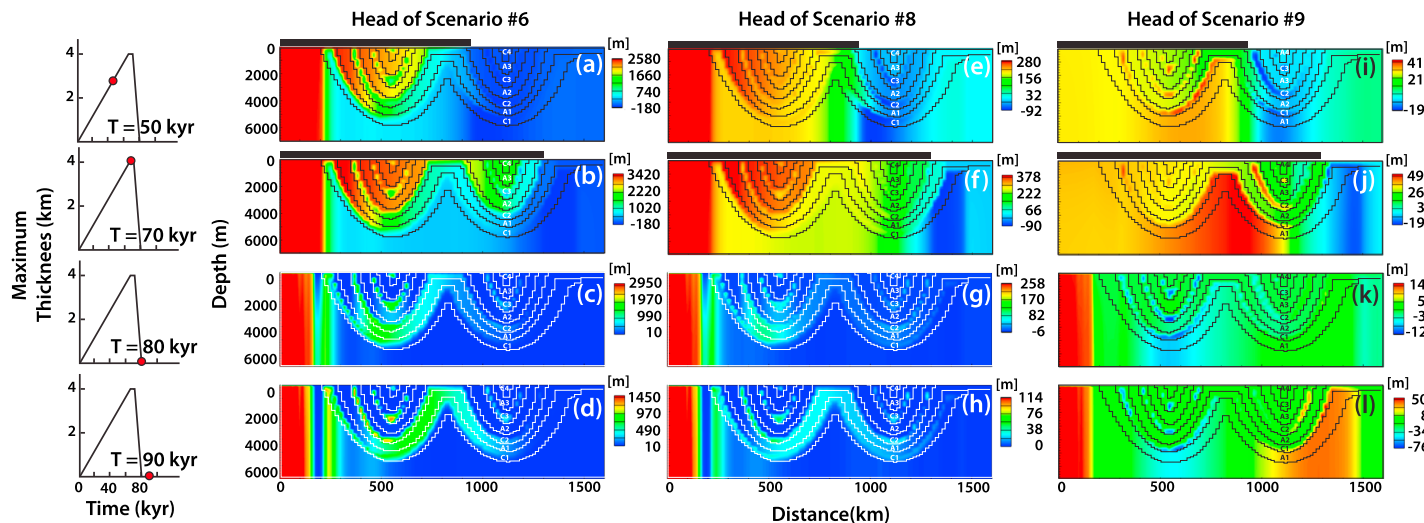


Figure 9. Computed heads of Scenario #6 (a–d), Scenario #8 (e–h), and Scenario #9 (i–l) after one glacial cycle. Black rectangles on the top of the model domain (a and b, e and f, and i–j) denote the lateral extension of the ice sheet. The red dots on the ice sheet evolution function on the left edge denote the time period at which the corresponding snapshot is taken. Note that each contour plot uses a different color scale. See Table 2 and text for detailed descriptions of different simulation scenarios.

Skempton's coefficient from 1 to 0.5 (Scenario #8; Figures 9e–9h), and a reversed stratigraphic order such that a basal aquifer overlies the crystalline basement (Scenario #9; Figures 9i–9l). Results in Figure 9 should be compared to the base case (Scenario #1) in Figures 8a–8d.

To isolate the geomechanical loading effects, we imposed no water table gradient across the top of the model domain and removed variable-density effects on computed freshwater hydraulic heads from the results in Figures 8 and 9. Variable-density effects due to fluid density increases with depth were included in calculations of groundwater velocities (equation (S9) in the supporting information) and advective-dispersive solute transport. However, they can result in freshwater hydraulic head increases up to 50 m near the bottom of the hydrologic model domain (see the supporting information, S4.3).

The first and second rows of Figures 8 and 9 show hydraulic head distributions during ice sheet growth and during LGM, respectively. The third and fourth rows show the head distributions at EoG and MOD, respectively. The lateral extent of the ice sheet is shown using the black rectangles on the top of select contour plots. Note that the color scales are different for each individual subplot in Figures 8 and 9, as head ranges differ significantly. The discontinuous nature of the computed head patterns in the confining units is due to local variations in confining unit thickness, which is the result of the *blocky* nature of the discretization shown in Figure 5a.

Throughout one glacial cycle, the head magnitude varied by about a factor of 2 between Scenarios #1 (Grolimund-Zoback rheology) and #3 (Lund-Wu rheology) although the overall patterns remain similar (compare Figures 8a–8d to Figures 8e–8h). We do not observe many differences in head patterns between 3-D loading (Scenario #1, Figures 8a–8d and Scenario #3, Figures 8e–8h) and 1-D loading (Scenario #5, Figures 8i–8l) except that 1-D loading does not give any head changes in front of the ice sheet terminus. Computed heads using the vertical loading rates are higher than either of the 3-D loading scenarios. For all three scenarios (#1, #3, and #5) heads build up within confining units and the underlying basement during the ice growth from $T = 50$ to 70 Kyr (Figures 8a and 8b, 8e–8f, and 8i–8j). Confining unit heads are highest below the middle of the ice sheet, which is not where either the 1-D or 3-D loading rates are highest (Figure 7). This can be understood in terms of the confining unit response times. The response time of a confining unit ($\tau = K_2 L^2 / S_2$) depends on the vertical hydraulic conductivity of the confining unit (K_2), the confining unit thickness (L), and the specific storage of the confining unit (S_2) and provides a time estimate for a confining unit to equilibrate in response to a sudden change in load. Given the range of confining unit thickness ($L = 500$ to 800 m), we estimate that the confining unit response time to ice sheet loading is between 80,000 and 200,000 years, generally longer than one glacial cycle. Thus, the computed heads in the confining unit are out of phase with the instantaneous loading rates. Computed heads within the aquifers are generally lower than in the adjacent confining units during ice sheet advance (Figure 8, upper two rows). Beyond the terminus of the ice sheet, heads in confining units are subhydrostatic for both Scenarios #1 and #3 during the ice sheet growth (Figures 8a and 8e). However, for the vertical loading scenario (Scenario #5), confining unit heads are zero beyond the ice sheet terminus (because $\frac{\partial \sigma_{yy}}{\partial t} = 0$) during the same period (Figure 8i).

We attributed these head patterns (high in confining units and lower in aquifers) to several factors. First, during ice sheet growth, the loading rates (i.e., internal source term in the groundwater flow equation) are positive underneath the ice sheet. They are either negative or zero near the terminus of the ice sheet. Second, the heads in low-permeability confining units and thick basement are more responsive to the mechanical loading effects than in the more permeable aquifers because the source term cannot be dissipated as quickly in shales. Lastly, computed heads within the aquifers are more strongly influenced by the upper specified head boundary conditions beneath the ice sheet but these are relatively low since they are only 10% of the ice sheet thickness.

At LGM, for Scenarios #1 and #3 (Figures 8b and 8f), the maximum heads are about 524 and 907 m within the basal confining unit (C1) underneath the ice sheet, in the connection part between two basins. In contrast, the maximum head (1,043 m) for Scenario #5 occurs in a region of the basal confining unit (C1) that is closer to the northern flank of the northern basin (Figure 8j). For all scenarios listed in Figure 8, as the ice sheet retreats following LGM (Figure 8, Row 3), negative heads develop primarily within the confining units and crystalline basement as the sign of the loading source term underneath the ice sheet flips from positive to negative. The head anomalies within the crystalline basement are mainly due to the low-permeability cap of the basal confining unit. At EoG, computed heads as low as -120 , -320 , and -460 m occur within the

confining units C2 and C3 along the central part of the north basin for Scenarios #1, #3, and #5, respectively (Figures 8c, 8g, and 8k). At MOD, the most negative heads have recovered to -85 , -246 , and -323 m, for Scenarios #1, #3, and #5, respectively (Figures 8d, 8h, and 8l), within basal confining unit (C1) at a depth of 700 m along the northern flank of the northern basin.

The effect of applying a 90% ice sheet thickness top boundary is evident in Figures 9a–9d (Scenario #6, Table 2). During the time from ice sheet growth to LGM, heads are highest in the aquifers (compare Figures 8a and 8b to Figures 9a and 9b). While the mechanical loading still plays a role in the simulated heads in the confining units for this scenario, anomalous negative pressures could not build up within the low-permeable confining units because the heads at the boundary of the confining units were much higher. Thus, at MOD, opposite head patterns dominate across the domain as was shown in Figure 9, with higher heads in the confining units and lower heads in the adjacent aquifers (compare Figures 8c and d to Figures 9c and 9d). Modern-day simulated heads are extraordinarily high ($>1,000$ m above hydrostatic conditions) within the confining units in formerly glaciated areas. We conclude that using an upper boundary condition of 90% of ice sheet thickness (Scenario #6) could produce the highest positive head (1,337 m) at MOD in the confining unit among all static permeability scenarios.

The effect of reducing the Skempton's coefficient (Scenario #8) from 1.0 to 0.5 can be seen by comparing Figures 9e–9h to Figures 8a–8d (Scenario #1). During ice growth until LGM, the impact of mechanical loading on the confining unit heads is diminished (Figures 9e and 9f). Similarly, during the unloading phase, the negative source term underneath the ice sheet will also be diminished. As a consequence, we see no negative heads in the confining units at MOD (Figure 9h).

The most profound impact of flipping the stratigraphy order from having a basal confining unit to having a basal aquifer overlying the basement (Scenario #9, Figures 9i–9l) can be seen from a broad region of high positive heads (up to 55 m) at MOD in the basal aquifer (A1) and in the underlying basement along the southern flank of in the southern basin (Figure 9l), which was not seen in Scenario #1 (Figure 8d).

3.5. Aquifer Groundwater Flow Patterns

We found that lateral simulated flow rates within the aquifer units did not vary much among Scenarios #1, #3, and #5. However, the choice of the upper hydraulic boundary condition (10% versus 90% of ice sheet thickness) did have an important impact on horizontal groundwater flow patterns and magnitudes (Q_x in m/yr). Figure 10 compares simulated lateral flow velocities for Scenarios #1 (10%) and #6 (90%). Positive values of groundwater velocity indicate flow from north to south (left to right). We added groundwater streamlines (lines with arrowheads) and stagnation points (circles) in the basal aquifer (A1) to help illustrate how flow direction changes through time. For Scenario #1, lateral groundwater flow patterns are complex and are controlled, to a large degree, by anomalous pressure formed in adjacent confining units. The lateral flows rates are relatively small (on the order of cm/yr) restricting advective-dispersive solute transport. During ice sheet growth ($T = 50, 70$ Kyr) in Scenario #1 (Figures 10a and 10b), the flow system in the basal aquifer includes multiple stagnation points of convergent or divergent flow. These shift through time as heads change within the confining units. The upper hydraulic head boundary condition also plays a role, but because its magnitude is only 10% of ice sheet height, it does not control aquifer flow. At LGM ($T = 70$ Kyr) flow patterns reverse as deglaciation begins and the internal source term becomes negative. With a specified head boundary of 90% of ice sheet height during the ice sheet growth in Scenario #6, groundwater flow rates are always southward away from the ice sheet and are about 2 orders of magnitude higher than the 10% case (>100 cm/yr; Figures 10e and 10f). This scenario promotes significant flushing of basinal brines. When the ice sheet disappears in Scenario #6, buoyancy effects associated with deep basinal brines drive flow back to the north, beginning in the northern basin (Figures 10g and 10h).

3.6. Vertical Head Profiles at MOD After 10 Cycles ($T = 990$ Kyr)

In Figure 11 we present the vertical head profiles at the center of the northern basin ($x = 560$ km; solid vertical line in Figure 5a) at the MOD after 10 cycles ($T = 990$ Kyr) for Scenarios #1–#7. For scenarios with a 10% ice sheet thickness top boundary (Scenarios #1–#5), underpressures are the most prominent features within the confining units and crystalline basement. This pattern is similar to what is observed at the Bruce site (Figure 1d; Neuzil & Provost, 2014). Of these static permeability Scenarios (#1, #3, and #5, Figure 11a), the most negative underpressures develop in Scenario #5 (dark green line in Figure 11a; vertical loading) and

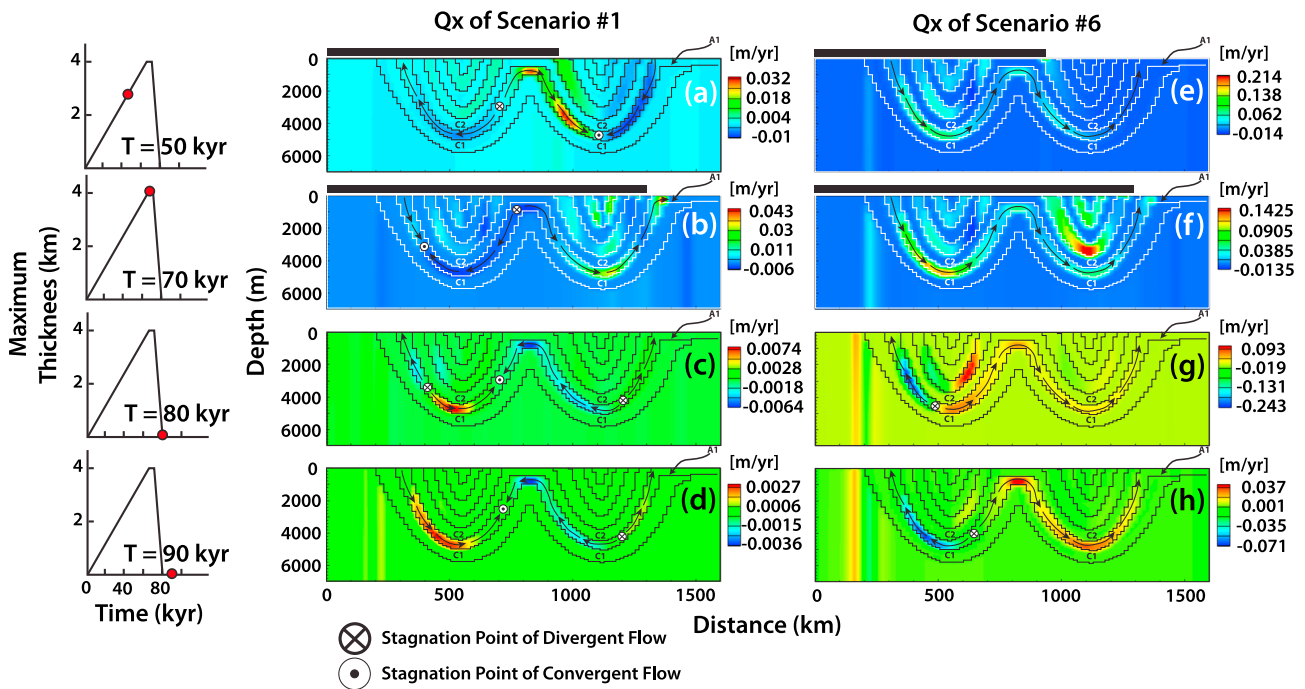


Figure 10. Spatial variations in lateral groundwater velocity (m/yr) for Scenario #1 (a–d) and Scenario #6 (e–h). Black rectangles on the top of the model domain denote the lateral extension of the ice sheet. The red dots on the ice sheet evolution function on the left edge denote the time period at which the corresponding snapshot is taken. Note that each velocity contour plot uses a different color scale. See Table 2 and text for detailed descriptions of different simulation scenarios.

the least negative ones in Scenario #1 (red line in Figure 11a; three-dimensional loading using the Grollmund-Zoback rheology). Underpressures within the aquifers become more negative with depth, which may be due to increasing hydrogeologic isolation. When failure-induced dynamic permeability conditions are considered (Scenarios #2 and #4, Figure 11b), underpressures are reduced in the confining units and decrease by about tenfold. Only overpressures are preserved in confining units when we set a 90% ice sheet thickness top boundary (Scenarios #6–#7, Figure 11c). Again, we see the effect of dynamic permeability reduces the magnitudes of anomalous heads (Scenario #7, brown line in Figure 11c).

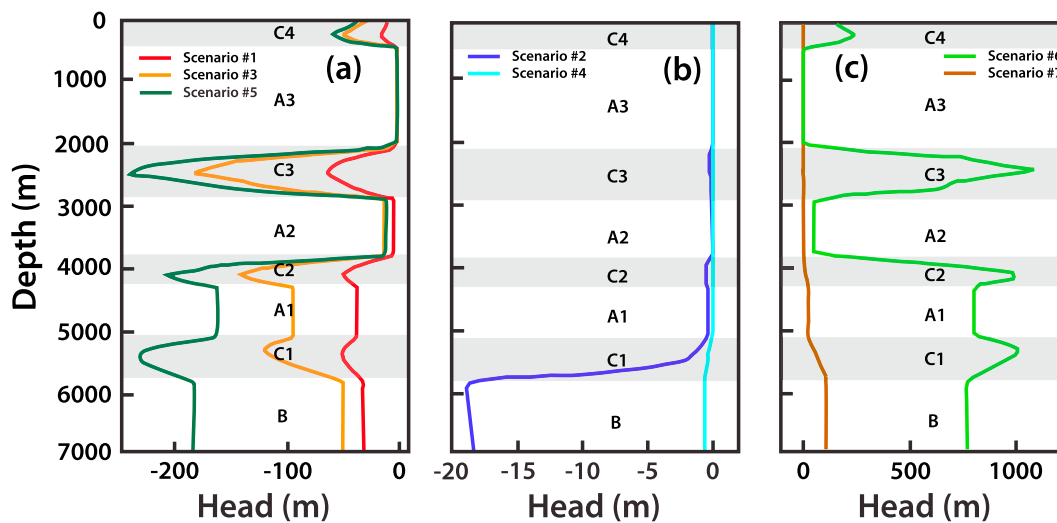


Figure 11. Comparison of the present-day (MOD) vertical head profiles after 10 glacial cycles (1 million years) extracted at $x = 560$ km (solid vertical line in Figure 5a) for (a) Scenario #1 (red line), Scenario #3 (orange line), and Scenario #5 (dark green line); (b) Scenario #2 (dark blue line) and Scenario #4 (light blue line); and (c) Scenario #6 (light green line) and Scenario #7 (brown line). Gray-shaded patterns represent are low permeable confining units, and white ones are aquifers and basement. See Table 2 and text for detailed descriptions of different simulation scenarios.

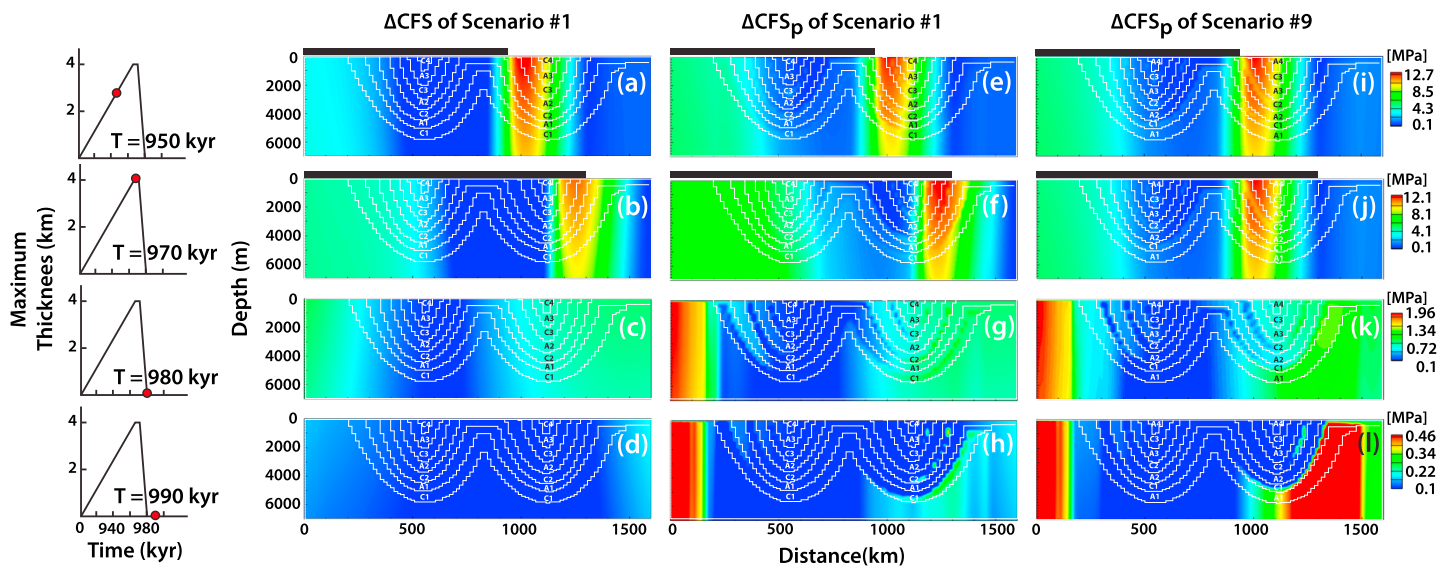


Figure 12. Comparison among simulated ΔCFS for Scenario #1 (left column, a–d), ΔCFS_p for Scenario #1 (middle column, e–h), and ΔCFS_p for Scenario #9 (right column, i–l) after 10 glacial cycles in unit of MPa. The cutoff values for both ΔCFS and ΔCFS_p are 0.1 MPa. Regions that are not blue are places that exceed the failure criterion. Black rectangles on the top of the model domain (a and b, e and f, and i–l) denote the lateral extension of the ice sheet. The red dots on the ice sheet evolution function on the left edge denote the time period at which the corresponding snapshot is taken. Note that the contours are in the same scales for each time period.

3.7. Comparison of Geomechanical Versus Hydromechanical Failure

Thus far, we have seen that hydraulic head (and hence pore pressure) changes are much smaller than geomechanical stress state changes due to glacial loading. This can be seen by comparing the vertical stress changes in Figure 6 to head changes in Figures 8 and 9 noting that 1 MPa is equal to a head change of 100 m. However, during interglacial periods, pore pressure changes become more important with respect to failure. Here we ask the question: Do pore pressures from Holocene to present day have a first-order effect on failure patterns using the ΔCFS_p criterion? Is there a hydromechanical *Wild Card* as postulated by Neuzil (2012)? Figure 12 compares and contrasts simulated failure (and hence seismicity) using the rheological properties consistent with Scenario #1 (Grollmund-Zoback rheology and Skempton's coefficient of 1). The first two columns of Figure 12 compare the geomechanical (ΔCFS , Figures 12a–12d) and hydrogeomechanical (ΔCFS_p , Figures 12e–12h) failure patterns across one glacial cycle for Scenario #1. The last column (Figures 12i–12l) shows hydromechanical (ΔCFS_p) failure patterns for Scenario #9, which flips the hydrostratigraphic order with a basal aquifer overlying the basement. All rows use the same contour interval. The computed anomalous heads (converted to pore pressures) used in the ΔCFS_p calculation in Figures 12e–12h and Figures 12i–12l are shown in Figures 8a–8d and Figures 9i–9l, respectively, as the heads almost repeated their evolution history every glacial cycle. We subtracted the imposed head at the top of each nodal column of the hydrologic model in our ΔCFS_p calculations. Overall, we conclude that changes in the failure region due to pore pressure increases are second order in nature during periods of glaciation (compare Figures 12a and 12b to Figures 12e and 12f). Head changes of a few hundred meters are much smaller than the flexural and vertical loads that can reach tens of MPa. However, from EoG to MOD, hydraulic heads begin to have a first-order effect on the extension of failure regions because glacially induced incremental stresses in the lithosphere dissipated as the ice sheet retreated (compare Figure 12c to Figure 12g for EoG, and compare Figure 12d to Figure 12h for MOD). At MOD, the hydromechanical failure metric (ΔCFS_p) exceeds the 0.1-MPa critical value in the basal confining unit (C1) of the southern basin, in the crystalline basement underneath the southern basin, and in the basement near the northern edge of the domain (Figure 12h). In contrast, the geomechanical failure region only appears at the southern and northern edges of the model domain (Figures 12c and 12d). The pattern of the hydromechanical failure is more or less consistent with the spatial distributions of the overpressures in the confining units and crystalline basement at MOD (compare Figure 12h to Figure 8d). With the flipped stratigraphy (Scenario

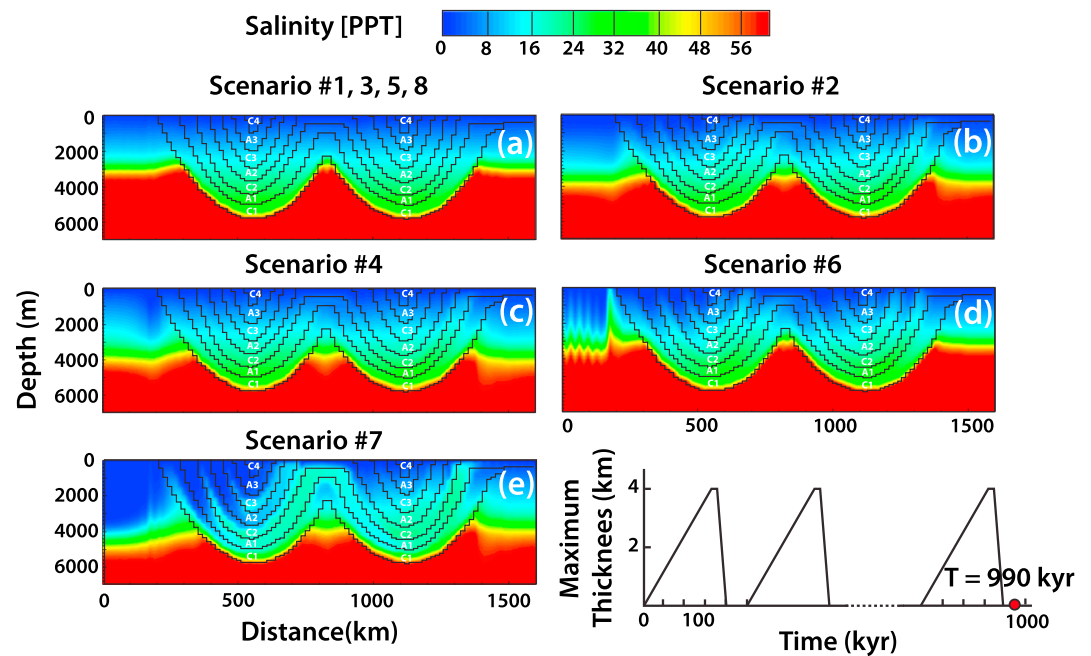


Figure 13. Contour plots of present-day (MOD) salinity patterns after 10 glacial cycles ($T = 990$ kyr) in units of parts per thousand (ppt) for (a) Scenarios #1, #3, #5, and #8 that are combined together; (b) Scenario #2; (c) Scenario #4; (d) Scenario #6; and (e) Scenario #7. The red dot on the ice sheet evolution function in the right bottom corner denotes the time period at which the snapshots are taken. The maximum salinity for all cases is 60 ppt. See Table 2 and text for detailed descriptions of different simulation scenarios.

#9), overpressures are more extensive and of a higher magnitude beyond the ice sheet terminus at MOD (Figure 9l). This is reflected in the larger extension of failure regions and higher magnitudes of ΔCFS_p beyond the ice sheet terminus in the basal aquifer (A1) and underlying basement (Figure 12l).

3.8. Simulated Salinity Patterns

The MOD salinity contours of selected scenarios after 10 glacial cycles are presented in Figure 13. We also extracted the horizontal salinity profiles across the hydrologic model domain at a fixed depth ($y = 1,500$ m; see dashed horizontal line in Figure 5a) into a concentration versus distance plot in Figure 14. All four static permeability scenarios that used an upper hydraulic head boundary condition of 10% of ice sheet thickness (Scenarios #1, #3, #5, and #8; Figures 13a and 14) did not produce significant asymmetric salinity patterns within aquifers or *flushing* (i.e., decreasing salinity to less than 1 ppt to a depth of 1.5 km along the northern flank of the northern basin in Aquifer A1). Only in dynamic permeability scenarios (Scenarios #2, #4, and #7; Figures 13b, 13c, and 13e) or when a 90% ice sheet thickness top boundary condition is imposed (Scenarios #6 and #7; Figures 13d and 13e) did significant flushing occur. Recharging glacial meltwater diluted the salinity along the northern flank of each basin, while upwelling of deeper basal brines raised salinity at the shallower depth along the southern limbs of each basin (Figures 13b–13e and 14). The greatest amount of flushing was observed when the 90% ice sheet thickness top boundary condition was imposed along with dynamic permeability (Scenario #7, Figures 13e and 14b). In contrast to other scenarios, salinity increases in the basal aquifer (A1) along the northern flank of the southern basin occurred in Scenario #7 (Figure 14b), as a consequence of interbasinal transport of solutes. All of the flushing scenarios mentioned above (Scenarios #2, #4, #6, and #7) produced characteristic asymmetric aquifer salinity patterns that are generally consistent with the Cl^- concentration contour map shown in Figures 1a and 1b with freshening occurring mainly along the northern margins and concentrating along the southern margin of each basin. Along the northern flank of the northern basin, confining unit salinity less than 1 ppt extends to a depth of 1,000 m in Scenarios #2, #4, #6, and #7.

Removal of solutes from confining units is the result of advective solute transport (see calculated Peclet numbers at monitoring point C1_MP1 Peclet numbers, Table 5) and solute diffusion (Hendry et al., 2013; Mazurek

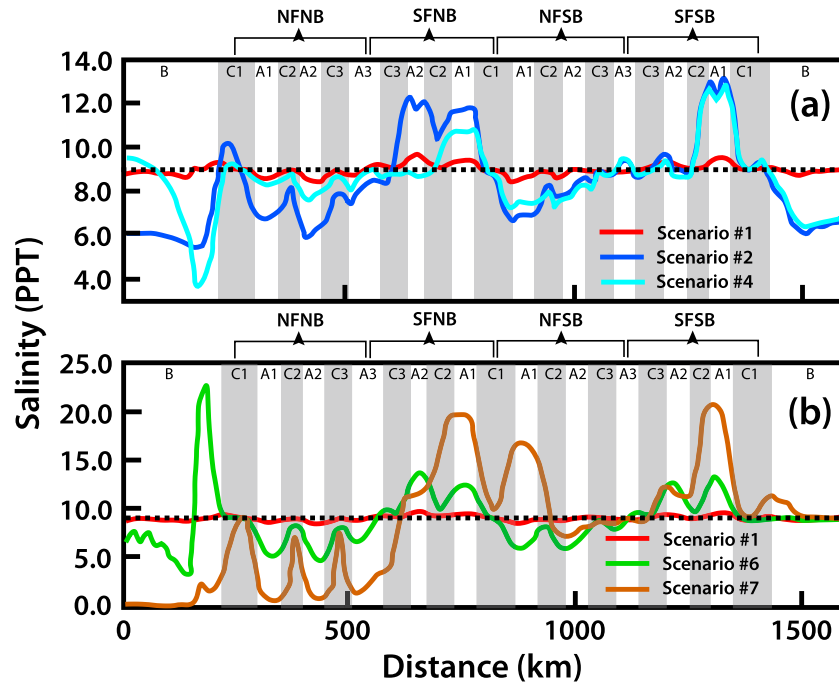


Figure 14. Comparison of the present-day (MOD) horizontal salinity profiles after 10 glacial cycles ($T = 990$ Kyr) extracted at the depth of 1,500 m in unit of parts per thousand (ppt) for (a) Scenario #1 (red line), Scenario #2 (dark blue line), and Scenario #4 (light blue line) and (b) Scenario #1 (red line), Scenario #6 (light green line), and Scenario #7 (brown line). NFNB stands for northern flank of northern basin, SFNB stands for southern flank of northern basin, NFSB stands for northern flank of southern basin, and SFSB stands for southern flank of southern basin. See Table 2 and text for detailed descriptions of different simulation scenarios.

et al., 2011). Peclet numbers for the dynamic permeability cases were as high as 94 (Scenario #7) within confining units at C1_MP1 (Table 5). For the static permeability cases, the vertical Peclet number for solute transport in the confining units was 0.01 or less (Table 5). Salinity evolution at three monitoring points (A1_MP1, A1_MP2, and A1_MP3, Figure 5a) within the basal aquifer (A1) is presented in section S4.5 in the supporting information. This shows that salinity values at various monitoring points never reached equilibrium or *dynamic* equilibrium after 10 cycles of glaciation.

4. Discussion

One of the most interesting findings of our study was that relatively high pore pressures (up to 50 m) within the crystalline basement are preserved today up to 150 km beyond the terminus of the ice sheet (see Figures 8d, 8h, 8l and Figures 9d, 9h, 9l), regardless of what parameters were used. Evidence for the existence

Table 5
Summary of Monitoring Points A1_MP1, C1_MP1, and C1_MP2

| Scenarios | A1_MP1 | | | | C1_MP1 | | | | C1_MP2 | | | | | |
|-----------|------------------|------------------|--------------|--------------|------------------|------------------|--------------|--------------|--------------------|------------------|------------------|--------------|--------------|--------------------|
| | Max v_x (m/yr) | Min v_x (m/yr) | Max Head (m) | Min Head (m) | Max v_z (m/yr) | Min v_z (m/yr) | Max Head (m) | Min Head (m) | Vertical Solute Pe | Max v_z (m/yr) | Min v_z (m/yr) | Max Head (m) | Min Head (m) | Vertical Solute Pe |
| 1 | 0.04 | -0.002 | 387 | -43 | 1.6e-6 | -1.3e-6 | 503 | -115 | 0.03 | 4.1e-7 | -6.0e-7 | 55 | -208 | 0.01 |
| 2 | 0.7 | -0.03 | 386 | -45 | 8.1e-5 | -9.1e-5 | 394 | -18 | 1.7 | 6.4e-5 | -3.4e-5 | 88 | -36 | 1.9 |
| 3 | 0.03 | -7.1e-4 | 387 | -87 | 3.9e-6 | -2.7e-6 | 606 | -243 | 0.08 | 8.5e-7 | -1.9e-6 | 132 | -428 | 0.03 |
| 4 | 3.0 | -0.07 | 386 | -18 | 6.6e-4 | -3.2e-4 | 468 | -5 | 14.1 | 9.4e-4 | -3.0e-4 | 62 | -19 | 28.3 |
| 5 | 0.03 | -0.011 | 387 | -19 | 7.3e-6 | -3.3e-6 | 956 | -391 | 0.2 | 5.0e-8 | -2.2e-7 | 9 | -2e-7 | 0.015 |
| 6 | 0.1 | -0.3 | 3475 | -38 | 6.8e-7 | -2.9e-5 | 1337 | -56 | 0.01 | 2.7e-7 | -6.2e-7 | 34 | -208 | 0.0082 |
| 7 | 6.3 | -1.1 | 3478 | -20 | 0.0044 | -8.0e-4 | 3506 | -16 | 94.4 | 1.1e-4 | -4.3e-5 | 102 | -35 | 2.3 |

of high excess pore pressures (>0.27 MPa) to a depth of up to 5 km below the land surface near the New Madrid seismic zone has been reported by McKeown and Diehl (1994).

Our study is not the first study to propose that Holocene and historical seismicity is related to Pleistocene glaciations (e.g., Grollmund & Zoback, 2001). When we compare the position of the failure region predicted by ΔCFS_p at MOD of either Scenario #1 or Scenario #9 in the cross section (Figures 12h and 12l) with the epicenters of the Holocene seismicity (from Wheeler & Cramer, 2002; red dots in Figure 1c), as well as historical earthquakes (brown dots in Figure 1c), we find that distances between the earthquake epicenters and the maximum lateral ice sheet extent qualitatively match the distances between the failure region and the maximum lateral ice sheet extent. In addition, Wu and Hasegawa (1996) also reported that the relatively tectonically *quiet* Baffin Island of Eastern Canada experienced large earthquakes up to $M7$, which is generally consistent with the position of our failure region located at the northern end of our model domain.

One specific goal of this study was to determine whether or not a single set of hydraulic boundary conditions, rheological properties, and petrophysical properties could produce basin-scale brine flushing and modern anomalous pore pressures that are consistent with field observations. We found that under the assumption of static permeability conditions using a tight confining unit permeability ($k_z = 10^{-20}$ m²) and intermediate permeability for the aquifer units ($k_x = 10^{-14}$ m²), our models generated subhydrostatic heads in deep confining units along the northern flank of sedimentary basins not unlike what is observed in natural systems (Neuzil & Provost, 2014). These patterns were found to be independent of the assumed rheological model, provided that the specified head boundary beneath the ice sheet, along the top of the solution domain, reached only 10% of the ice sheet thickness. This relatively low hydrologic head boundary condition could be plausible if a thick till layer overlies the sedimentary basin aquifers. However, modern field observations of hydraulic head conditions beneath southwestern Greenland ice sheet reported by Claesson Liljedahl et al. (2016) suggest that groundwater heads are closer to floating conditions (90% of ice sheet height). This field site has little to no till units. Consistent with Khader and Novakowski (2014), we found that imposing floating conditions beneath the ice sheet eliminated modern-day under pressures in shales.

Underpressures were not preserved in the dynamic permeability scenario. Given that there are numerous field sites where anomalous pore pressures are preserved (Neuzil, 2013) and diffusional salinity profiles exist in tight confining units (Mazurek et al., 2011; Neuzil & Provost, 2014), we hypothesize that failures through shales must occur along discrete preexisting planes of weakness such as fault zones rather than broad failure regions as we assumed in this study. The idea of failure occurring along discrete fault planes through confining units has been observed in one field setting. In order to account for water level fluctuations in a paired confined-unconfined aquifer system in Taiwan following the $M7.6$ Chi-Chi earthquake, Wang et al. (2016) concluded that coseismic breach of confining units occurred about 10% of the time along discrete failure surfaces.

A static aquifer permeability of 10^{-14} m² (k_x) did not produce brine flushing in aquifers in our models. Had we used a higher aquifer permeability, say 10^{-12} m², we would have achieved both aquifer salinity flushing and underpressure formation in tight confining units. However, a permeability of 10^{-12} m² is higher than most values reported for aquifer systems in the Michigan (Gupta & Bair, 1997) and Illinois Basins (Bethke et al., 1991).

Using a critical failure threshold of 0.1 MPa for ΔCFS_p and typical aquifer (10^{-14} m²) and relatively tight confining unit (10^{-20} m²) permeabilities, we found that permeability changes (100-fold increase) could lead to enhanced brine flushing within sedimentary basin aquifers over many glacial cycles (~ 10). One or two glacial cycles were not able to cause significant flushing (see Figure S10 in the supporting information). Temporal changes in aquifer salinity at a given location were complex (Figure S10). Our results suggest that salinity patterns in sedimentary basins do not reach dynamic equilibrium conditions in response to modern or Pleistocene hydrologic forcing even over a time period of 1 million years. Future studies might approach this question in the form of an inverse analysis (e.g., Bethke, 1986): How high must aquifer permeability be to account for observed brine flushing in formerly glaciated sedimentary basins?

Our lithosphere geodynamic model in response to ice sheet loading is relatively simple when compared to those developed by the geodynamic community (e.g., Steffen et al., 2014; Wu, 1992, 2004). We used an elastic representation of the lithosphere. We did not take into account the advection of prestress as Wu (2004) did.

Viscous asthenosphere flow was represented using a time-varying displacement boundary condition along the lithosphere's bottom boundary (Van der Veen, 1999). We did not consider convective effects of groundwater flow on permafrost evolution (McKenzie et al., 2007; Walvoord et al., 2012). We only permitted bulk permeability enhancement to persist as long as the Mohr-Coulomb failure criterion was exceeded. We assumed that permeability decreased back to prefailure levels instantaneously (although using 100-year time steps, this assumption seems consistent with postseismic thermal and hydrologic observations within watersheds; Manga et al., 2012). Failure along individual fault planes was not considered (e.g., Murphy et al., 2013; Steffen et al., 2014); instead, we enhanced the permeability of a broad region wherever the failure criteria (ΔCFS_p) is met. Finally, it is worth noting that even though each physical process was represented in a relatively a simplified manner, the integrated analysis is complex and likely nonunique.

We further recognize that the heterogeneous and faulted shallow crust might not be well presented as a homogeneous isotropic mechanical continuum. Regional faults in particular could potentially change the mechanical behavior of the rocks (e.g., Wu & Hasegawa, 1996). The poorly constrained ice sheet evolution model and our relatively simple lithosphere and asthenosphere render the stress calculation uncertain (Neuzil & Provost, 2014; Wu, 2013). We recognize from marine isotopic records that the Laurentide ice sheet evolution history is far more complex than represented by our idealized model. Additionally, the permeability of the Illinois and Michigan Basins is heterogeneous and likely depth dependent, which was not considered. Lastly, we assumed that the permeability enhancement was shear failure triggered on one particular fault orientation (30° from σ_1). In nature, numerous fault planes with different orientations and different failure probabilities exist. As a consequence, our study is of a conceptual nature and our comparisons to field conditions are qualitative.

One reviewer (C. E. Neuzil) pointed out that only two field sites (the Bruce Site in Canada and the Wellenberg Site in Switzerland) have well-documented measurements of underpressures related to deglaciation. Other instances of underpressure phenomena reported in tight confining units could be due to other mechanisms such as erosional unloading (Corbet & Bethke, 1992) and osmosis effects (Greenberg et al., 1973; Neuzil & Person, 2017). Additional careful field campaigns measuring pore pressures in tight confining units in formerly glaciated terrains seems warranted.

5. Conclusions

Using a new multiphysics numerical model developed as part of this study (Figure 4), we assessed how differences in lithospheric rheological (Grollimund & Zoback, 2000; Lund, 2005; Wu, 1992) and petrophysical properties (permeability) and hydraulic boundary conditions affect Pleistocene groundwater flow patterns, pore pressure evolution, and flushing of sedimentary basin brines. Our study is among the first to consider how hydromechanical failure influences basin-scale dynamic permeability evolution (e.g., Rojstaczer et al., 2008) and solute flushing in aquifers during Pleistocene glacial loading.

During glacial loading, pore pressure increases appear to play a secondary role on failure as the stress components induced by ice sheet loading are much larger than the pore pressure component in ΔCFS_p calculations. However, during the Holocene to modern times after the ice sheet disappeared, pore pressures became the most dominant factor in determining the failure in the subsurface. We observed a broad failure region delineated by ΔCFS_p , which occurs within the crystalline basement rocks and confining units up to 150 km beyond the ice sheet and in the Arctic region (Figures 12h and 12l). This is in the same general area as the New Madrid seismic zone (Figure 1c; Grollimund & Zoback, 2001) and is also consistent with modern seismicity recorded around Hudson Bay, eastern Canada (Wu & Hasegawa, 1996), as well as the Holocene seismicity beneath the center of the Fennoscandian Ice Sheet that has been observed in the Scandinavia region (Arvidsson, 1996; Lagerbäck, 1978; Wood, 1989). It is important to note, however, that these simulated failure predictions do not take into account modern, large tectonic stresses (Heidbach et al., 2010; Zoback & Zoback, 1989). In addition, critically stressed faults will have different orientation under different tectonic stress fields (Lund, 2005, 2015; Lund et al., 2009). Consideration of modern tectonic stress fields would likely complicate the findings presented above.

We found that using one-dimensional vertical loading with a Skempton's coefficient of 1.0 resulted in the highest fluid overpressure and underpressure formation, followed by the three-dimensional loading

scheme using the Lund-Wu rheology (Table 1) with the Grollmund-Zoback rheology yielding the lowest levels of anomalous pore pressures.

Brine flushing (lowering salinity of aquifers below 1 ppt at depth > 1.5 km along the northern margins of the northern basin) occurred when aquifer permeabilities were increased from 10^{-14} m² to 10^{-12} m² due to shear failure. However, increasing permeability of confining units by a factor of 100 removed underpressures. Since diffusional dominated solute profiles (Mazurek et al., 2011) and underpressured tight confining units (Neuzil, 2013) are more the rule than the exception, we hypothesize that permeability enhancement due to shear failure, if it occurs in shales, must occur along discrete fault planes rather than modifying bulk confining unit permeability at a basin scale.

Acknowledgments

This study was supported by NSF grant (Mark Person EAR-1344553 and NSF EPSCoR under grant IIA-130134 and Jennifer McIntosh EAR-0635685). The authors are grateful to Editor Jean Bahr, Associate Editor Larry Murdoch, Dr. Chris Neuzil, and two anonymous reviewers who helped us greatly improve the manuscript. Thanks to Dr. Alex Rinehart for helpful discussions about adopting the Mohr-Coulomb failure criteria. Our model package (CVFEM_Rift2D) has been uploaded onto the CSDMS (Community Surface Dynamics Modeling System) website hosted by the University of Colorado (https://csdms.colorado.edu/wiki/Model_download_portal). The users can download the package by selecting Hydrological Models in the Model Repository Menu and searching for CVFEM_Rift2D. The uploaded files include (1) MATLAB-based control volume finite element two-dimensional geomechanical model *cvfem_ice.m*, (2) Fortran-based two-dimensional flow and transport model *Rift2D*, and (3) MATLAB-based one-dimensional permafrost model *permafrost_ice.m*. The grid generation and model input parameters for the geomechanical model are contained within the MATLAB-based codes. Information on how to modify the input parameters, grid sizes, and boundary conditions can be found in the file *readme_cvfem_ice.txt*. Information on running Rift2D and creating data sets can be found in the uploaded Rift2D model documentation and graphical preprocessor. Rift2D can be compiled using gfortran. Rift2D and *cvfem_ice.m* create Tecplot formatted output files that can be graphically rendered using either Tecplot or Pareview. The program *permafrost_ice.m* generates the subsurface temperature profiles in a txt file every 1,000 years for the entire 100,000-year cycle for each individual column.

References

- Archer, D., & Ganopolski, A. (2005). A movable trigger: Fossil fuel CO₂ and the onset of the next glaciation. *Geochemistry, Geophysics, Geosystems*, 6, Q05003. <https://doi.org/10.1029/2004GC000891>
- Arvidsson, R. (1996). Fennoscandian earthquakes: Whole crustal rupturing related to postglacial rebound. *Science*, 274(5288), 744–746. <https://doi.org/10.1126/science.274.5288.744>
- Bahr, J. M., Moline, G. R., & Nadon, G. C. (1994). Anomalous pressures in the Michigan Basin. In P. J. Ortoleva & P. Westcott (Eds.), *Basin compartments and seals, American Association of Petroleum Geologists Memoir* (Vol. 61, pp. 153–165).
- Batzle, M., & Wang, Z. (1992). Seismic properties of pore fluids. *Geophysics*, 57(11), 1396–1408. <https://doi.org/10.1190/1.1443207>
- Bense, V. F., & Person, M. A. (2008). Transient hydrodynamics within intercratonic sedimentary basins during glacial cycles. *Journal of Geophysical Research*, 113, F04005. <https://doi.org/10.1029/2007JF000969>
- Bethke, C. M. (1986). Inverse hydrologic analysis of the distribution and origin of Gulf Coast-type geopressured zones. *Journal of Geophysical Research*, 91(B6), 6535–6545. <https://doi.org/10.1029/JB091iB06p06535>
- Bethke, C. M., Reed, J. D., & Oltz, D. F. (1991). Long-range petroleum migration in the Illinois Basin (1). *AAPG Bulletin*, 75(5), 925–945.
- Bletzinger, K. U., Bischoff, M., & Ramm, E. (2000). A unified approach for shear-locking-free triangular and rectangular shell finite elements. *Computers & Structures*, 75(3), 321–334. [https://doi.org/10.1016/S0045-7949\(99\)00140-6](https://doi.org/10.1016/S0045-7949(99)00140-6)
- Bluemle, J. P. (1993). Hydrodynamic blowouts in North Dakota. In J. S. Aber (Ed.), *Glaciotectonics and mapping glacial deposits, Canadian Plains Research Centre* (pp. 259–266). Regina, Saskatchewan: University of Regina.
- Boulton, G. S., & Caban, P. (1995). Groundwater flow beneath ice sheets: Part II—Its impact on glacier tectonic structures and moraine formation. *Quaternary Science Reviews*, 14(6), 563–587. [https://doi.org/10.1016/0277-3791\(95\)00058-W](https://doi.org/10.1016/0277-3791(95)00058-W)
- Bredehoeft, J. D., England, A. W., Stewart, D. B., Trask, N. J., & Winograd, I. J. (1978). *Geologic disposal of high-level radioactive wastes: Earth-science perspectives*. Reston, VA: US Geological Survey.
- Christiansen, E. A. (1967). Collapse structures near Saskatoon, Saskatchewan, Canada. *Canadian Journal of Earth Sciences*, 4(5), 757–767. <https://doi.org/10.1139/e67-053>
- Christiansen, E. A., Gendzwil, D. J., & Meneley, W. A. (1982). Howe Lake: A hydrodynamic blowout structure. *Canadian Journal of Earth Sciences*, 19(6), 1122–1139. <https://doi.org/10.1139/e82-097>
- Christiansen, E. A., & Sauer, E. K. (2001). Stratigraphy and structure of a Late Wisconsinan salt collapse in the Saskatoon Low, south of Saskatoon, Saskatchewan, Canada: An update. *Canadian Journal of Earth Sciences*, 38(11), 1601–1613. <https://doi.org/10.1139/e01-038>
- Claesson Liljedahl, L., Kontula, A., Harper, J., Näslund, J. O., Selroos, J. O., & Pitkänen, P., et al. (2016). The Greenland Analogue Project: Final report. SKB TR-14e13. Swedish Nuclear Fuel and Waste Management Co.(SKB), Stockholm, Sweden. Retrieved from <http://www.skb.se/publikation/2484498/>
- Cohen, D. (2015). Ice flow dynamic over Switzerland around the last glacial maximum, Tech. rep., NAGRA, NAB 15–22, Wettlingen, Switzerland, 144p
- Cohen, D., Gillet-Chaulet, F., Haerberli, W., Machguth, H., & Fischer, U. H. (2018). Numerical reconstructions of the flow and basal conditions of the Rhine glacier, European Central Alps, at the Last Glacial Maximum. *Cryosphere*, 12(8).
- Cohen, D., Person, M., Wang, P., Gable, C. W., Hutchinson, D., Marksamer, A., et al. (2010). Origin and extent of fresh paleowaters on the Atlantic continental shelf, USA. *Groundwater*, 48(1), 143–158. <https://doi.org/10.1111/j.1745-6584.2009.00627.x>
- Corbet, T. F., & Bethke, C. M. (1992). Disequilibrium fluid pressures and groundwater flow in the Western Canada sedimentary basin. *Journal of Geophysical Research*, 97(B5), 7203–7217. <https://doi.org/10.1029/91JB02993>
- Cutler, P. M., MacAyeal, D. R., Mickelson, D. M., Parizek, B. R., & Colgan, P. M. (2000). A numerical investigation of ice-lobe–permafrost interaction around the southern Laurentide ice sheet. *Journal of Glaciology*, 46(153), 311–325. <https://doi.org/10.3189/172756500781832800>
- De Marsily, G. (1986). *Quantitative hydrogeology*. Fontainebleau: Paris School of Mines.
- Ellis, A. J., & Mahon, W. A. J. (1964). Natural hydrothermal systems and experimental hot-water/rock interactions. *Geochimica et Cosmochimica Acta*, 28(8), 1323–1357. [https://doi.org/10.1016/0016-7037\(64\)90132-2](https://doi.org/10.1016/0016-7037(64)90132-2)
- Ellis, A. J., & Mahon, W. A. J. (1967). Natural hydrothermal systems and experimental hot water/rock interactions (Part II). *Geochimica et Cosmochimica Acta*, 31(4), 519–538. [https://doi.org/10.1016/0016-7037\(67\)90032-4](https://doi.org/10.1016/0016-7037(67)90032-4)
- Freeze, R. A., & Cherry, J. A. (1979). *Groundwater* (Vol. 604, pp. 215–21227). New Jersey: Prentice—Hall, Inc Englewood cliffs.
- Gambolati, G., Teatini, P., Baù, D., & Ferronato, M. (2000). Importance of poroelastic coupling in dynamically active aquifers of the Po river basin, Italy. *Water Resources Research*, 36(9), 2443–2459. <https://doi.org/10.1029/2000WR000127>
- Ge, S., & Garven, G. (1992). Hydromechanical modeling of tectonically driven groundwater flow with application to the Arkoma foreland basin. *Journal of Geophysical Research*, 97(B6), 9119–9144. <https://doi.org/10.1029/92JB00677>
- Ge, S., Liu, M., Lu, N., Godt, J. W., & Luo, G. (2009). Did the Zippingpu reservoir trigger the 2008 Wenchuan earthquake? *Geophysical Research Letters*, 36, L20315. <https://doi.org/10.1029/2009GL040349>
- Gendzwil, D. J., & Hajnal, Z. (1971). Seismic investigation of the Crater Lake collapse structure in southeastern Saskatchewan. *Canadian Journal of Earth Sciences*, 8(12), 1514–1524. <https://doi.org/10.1139/e71-141>
- Grapenthin, R. (2014). CRUSDE: A plug-in based simulation framework for composable CRUSTal DEformation studies using Green's functions. *Computers & Geosciences*, 62, 168–177. <https://doi.org/10.1016/j.cageo.2013.07.005>

- Grasby, S., Osadetz, K., Betcher, R., & Render, F. (2000). Reversal of the regional-scale flow system of the Williston basin in response to Pleistocene glaciation. *Geology*, 28(7), 635–638. [https://doi.org/10.1130/0091-7613\(2000\)28<635:ROTRFS>2.0.CO;2](https://doi.org/10.1130/0091-7613(2000)28<635:ROTRFS>2.0.CO;2)
- Grasby, S. E., & Chen, Z. (2005). Subglacial recharge into the Western Canada Sedimentary Basin—Impact of Pleistocene glaciation on basin hydrodynamics. *Geological Society of America Bulletin*, 117(3), 500–514. <https://doi.org/10.1130/B25571.1>
- Green, D. H., & Wang, H. F. (1986). Fluid pressure response to undrained compression in saturated sedimentary rock. *Geophysics*, 51(4), 948–956. <https://doi.org/10.1190/1.1442152>
- Greenberg, J. A., Mitchell, J. K., & Witherspoon, P. A. (1973). Coupled salt and water flows in a groundwater basin. *Journal of Geophysical Research*, 78(27), 6341–6353. <https://doi.org/10.1029/JC078i027p06341>
- Grollmund, B., & Zoback, M. D. (2000). Post glacial lithospheric flexure and induced stresses and pore pressure changes in the northern North Sea. *Tectonophysics*, 327(1–2), 61–81. [https://doi.org/10.1016/S0040-1951\(00\)00162-1](https://doi.org/10.1016/S0040-1951(00)00162-1)
- Grollmund, B., & Zoback, M. D. (2001). Did deglaciation trigger intraplate seismicity in the New Madrid seismic zone? *Geology*, 29(2), 175–178. [https://doi.org/10.1130/0091-7613\(2001\)029<0175:DDTISI>2.0.CO;2](https://doi.org/10.1130/0091-7613(2001)029<0175:DDTISI>2.0.CO;2)
- Gupta, N., & Bair, E. S. (1997). Variable-density flow in the midcontinent basins and arches region of the United States. *Water Resources Research*, 33(8), 1,785–1,802. <https://doi.org/10.1029/97WR01199>
- Haas, C. J., Touloukian, Y. S., Judd, W. R., & Roy, R. F. (1989). Static stress-strain relationships. *Physical Properties of Rocks and Minerals*, 2, 123–176.
- Hallet, B. (2011). Glacial erosion assessment. *Nuclear Waste Management Organization Report NWMO DGR-TR-2011-18*.
- Hanor, J. S. (1979). The sedimentary genesis of hydrothermal fluids. *Geochemistry of hydrothermal ore deposits*.
- Hanor, J. S., & McIntosh, J. C. (2006). Are secular variations in seawater chemistry reflected in the compositions of basinal brines? *Journal of Geochemical Exploration*, 89(1–3), 153–156. <https://doi.org/10.1016/j.gexplo.2005.11.054>
- Heidbach, O., Tingay, M., Barth, A., Reinecker, J., Kurfel, D., & Müller, B. (2010). Global crustal stress pattern based on the World Stress Map database release 2008. *Tectonophysics*, 482(1–4), 3–15. <https://doi.org/10.1016/j.tecto.2009.07.023>
- Hendry, M. J., Barbour, S. L., Novakowski, K., & Wassenaar, L. I. (2013). Paleohydrogeology of the Cretaceous sediments of the Williston Basin using stable isotopes of water. *Water Resources Research*, 49, 4,580–4,592. <https://doi.org/10.1002/wrcr.20321>
- Hendry, M. J., Solomon, D. K., Person, M., Wassenaar, L. I., Gardner, W. P., Clark, I. D., et al. (2015). Can argillaceous formations isolate nuclear waste? Insights from isotopic, noble gas, and geochemical profiles. *Geofluids*, 15(3), 381–386. <https://doi.org/10.1111/gfl.12132>
- Imbrie, J., Hays, J. D., Martinson, D. G., McIntyre, A., Mix, A. C., Morley, J. J., et al. (1984). The orbital theory of Pleistocene climate: Support from a revised chronology of the marine $\delta^{18}O$ record. In *Milankovitch and climate* (pp. 269–305). Boston, Massachusetts: D. Reidel Publishing Company.
- Ingebritsen, S. E., & Manning, C. E. (2010). Permeability of the continental crust: Dynamic variations inferred from seismicity and metamorphism. *Geofluids*, 10(1–2), 193–205.
- Ingebritsen, S. E., Sanford, W. E., & Neuzil, C. E. (2006). *Groundwater in geologic processes*. New York: Cambridge University Press.
- Iverson, N., & Person, M. (2012). Glacier-bed geomorphic processes and hydrologic conditions relevant to nuclear waste disposal. *Geofluids*, 12(1), 38–57. <https://doi.org/10.1111/j.1468-8123.2011.00355.x>
- Johnsen, S. J., Dahl-Jensen, D., Dansgaard, W., & Gundestrup, N. (1995). Greenland palaeotemperatures derived from GRIP bore hole temperature and ice core isotope profiles. *Tellus Series B: Chemical and Physical Meteorology*, 47(5), 624–629. <https://doi.org/10.3402/tellusb.v47i5.16077>
- Johnston, P., Wu, P., & Lambeck, K. (1998). Dependence of horizontal stress magnitude on load dimension in glacial rebound models. *Geophysical Journal International*, 132(1), 41–60.
- Khader, O., & Novakowski, K. (2014). Impacts of Pleistocene glacial loading on abnormal pore-water pressure in the eastern Michigan Basin. *Geofluids*, 14(2), 200–220. <https://doi.org/10.1111/gfl.12074>
- Kim, S. J., Crowley, T. J., Erickson, D. J., Govindasamy, B., Duffy, P. B., & Lee, B. Y. (2008). High-resolution climate simulation of the last glacial maximum. *Climate Dynamics*, 31(1), 1–16. <https://doi.org/10.1007/s00382-007-0332-z>
- King, G. C., Stein, R. S., & Lin, J. (1994). Static stress changes and the triggering of earthquakes. *Bulletin of the Seismological Society of America*, 84(3), 935–953.
- Kleinberg, R. L., & Griffin, D. D. (2005). NMR measurements of permafrost: Unfrozen water assay, pore-scale distribution of ice, and hydraulic permeability of sediments. *Cold Regions Science and Technology*, 42(1), 63–77. <https://doi.org/10.1016/j.coldregions.2004.12.002>
- Klemann, V., & Wolf, D. (1998). Modelling of stresses in the Fennoscandian lithosphere induced by Pleistocene glaciations. *Tectonophysics*, 294(3–4), 291–303. [https://doi.org/10.1016/S0040-1951\(98\)00107-3](https://doi.org/10.1016/S0040-1951(98)00107-3)
- Konikow, L. F., & Grove, D. B. (1977). Derivation of equations describing solute transport in ground water (No. 77–19). US Geological Survey, Water Resources Division.
- Lagerbäck, R. (1978). Neotectonic structures in northern Sweden. *Geologiska Föreningen i Stockholm Förhandlingar*, 100(3), 263–269. <https://doi.org/10.1080/11035897809452533>
- Lemieux, J. M., Sudicky, E. A., Peltier, W. R., & Tarasov, L. (2008a). Dynamics of groundwater recharge and seepage over the Canadian landscape during the Wisconsinian glaciation. *Journal of Geophysical Research*, 113, F01011. <https://doi.org/10.1029/2007JF000838>
- Lemieux, J. M., Sudicky, E. A., Peltier, W. R., & Tarasov, L. (2008b). Simulating the impact of glaciations on continental groundwater flow systems: 1. Relevant processes and model formulation. *Journal of Geophysical Research*, 113, F03017. <https://doi.org/10.1029/2007JF000928>
- Lemieux, J. M., Sudicky, E. A., Peltier, W. R., & Tarasov, L. (2008c). Simulating the impact of glaciations on continental groundwater flow systems: 2. Model application to the Wisconsinian glaciation over the Canadian landscape. *Journal of Geophysical Research*, 113, F03018. <https://doi.org/10.1029/2007JF000929>
- Lund, B. (2005). Effects of deglaciation on the crustal stress field and implications for end glacial faulting: A parametric study of simple Earth and ice models. SKB Technical Report TR-05-04, Uppsala, Svensk Kärnbränslehantering AB, 106 p. Retrieved from <http://www.skb.se/upload/publications/pdf/TR-05-04.pdf>
- Lund, B. (2015). Palaeoseismology of glaciated terrain. In *Encyclopedia of earthquake engineering* (pp. 1–16). Berlin Heidelberg: Springer. https://doi.org/10.1007/978-3-642-36197-5_25-1
- Lund, B., Schmidt, P., & Hieronymus, C. (2009). Stress evolution and fault stability during the Weichselian glacial Cycle SKB Technical Report TR-09-15, Uppsala, Svensk Kärnbränslehantering AB, 106 p. Retrieved from http://www.iaea.org/inis/collection/NCLCollectionStore/_Public/41/021/41021984.pdf
- Manga, M., Beresnev, I., Brodsky, E. E., Elkhoury, J. E., Elsworth, D., Ingebritsen, S. E., et al. (2012). Changes in permeability caused by transient stresses: Field observations, experiments, and mechanisms. *Reviews of Geophysics*, 50, RG2004. <https://doi.org/10.1029/2011RG000382>
- Marshall, S. J., James, T. S., & Clarke, G. K. (2002). North American ice sheet reconstructions at the Last Glacial Maximum. *Quaternary Science Reviews*, 21(1–3), 175–192. [https://doi.org/10.1016/S0277-3791\(01\)00089-0](https://doi.org/10.1016/S0277-3791(01)00089-0)

- Martini, A. M., Walter, L. M., Budai, J. M., Ku, T. C. W., Kaiser, C. J., & Schoell, M. (1998). Genetic and temporal relations between formation waters and biogenic methane: Upper Devonian Antrim Shale, Michigan Basin, USA. *Geochimica et Cosmochimica Acta*, 62(10), 1699–1720. [https://doi.org/10.1016/S0016-7037\(98\)00090-8](https://doi.org/10.1016/S0016-7037(98)00090-8)
- Mazurek, M., Alt-Epping, P., Bath, A., Gimmi, T., Waber, H. N., Buschaert, S., et al. (2011). Natural tracer profiles across argillaceous formations. *Applied Geochemistry*, 26(7), 1035–1064. <https://doi.org/10.1016/j.apgeochem.2011.03.124>
- McBride, J. H., Leetaru, H. E., Bauer, R. A., Tingey, B. E., & Schmidt, S. E. (2007). Deep faulting and structural reactivation beneath the southern Illinois basin. *Precambrian Research*, 157(1–4), 289–313. <https://doi.org/10.1016/j.precamres.2007.02.020>
- McIntosh, J. C., Garven, G., & Hanor, J. S. (2011). Impacts of Pleistocene glaciation on large-scale groundwater flow and salinity in the Michigan Basin. *Geofluids*, 11(1), 18–33. <https://doi.org/10.1111/j.1468-8123.2010.00303.x>
- McIntosh, J. C., Schlegel, M. E., & Person, M. (2012). Glacial impacts on hydrologic processes in sedimentary basins: Evidence from natural tracer studies. *Geofluids*, 12(1), 7–21. <https://doi.org/10.1111/j.1468-8123.2011.00344.x>
- McIntosh, J. C., & Walter, L. M. (2006). Paleowaters in Silurian-Devonian carbonate aquifers: Geochemical evolution of groundwater in the Great Lakes region since the Late Pleistocene. *Geochimica et Cosmochimica Acta*, 70(10), 2454–2479. <https://doi.org/10.1016/j.gca.2006.02.002>
- McKenzie, J. M., Voss, C. I., & Siegel, D. I. (2007). Groundwater flow with energy transport and water–ice phase change: Numerical simulations, benchmarks, and application to freezing in peat bogs. *Advances in Water Resources*, 30(4), 966–983. <https://doi.org/10.1016/j.advwatres.2006.08.008>
- McKeown, F. A., & Diehl, S. (1994). Evidence of contemporary and ancient excess fluid pressure in the New Madrid seismic zone of the Reelfoot Rift, central United States. In K. M. Shedlock & A. C. Johnston (Eds.), *Investigations of the New Madrid Seismic Zone, U.S. Geol. Surv. Prof. Pap. 1538-N* (pp. N1–N24). Reston, VA: US Geological Survey.
- Murphy, S., O'Brien, G. S., McCloskey, J., Bean, C. J., & Nalbant, S. (2013). Modelling fluid induced seismicity on a nearby active fault. *Geophysical Journal International*, 194(3), 1613–1624. <https://doi.org/10.1093/gji/ggt174>
- Neuzil, C. E. (1993). Low fluid pressure within the Pierre Shale: A transient response to erosion. *Water Resources Research*, 29(7), 2,007–2,020. <https://doi.org/10.1029/93WR00406>
- Neuzil, C. E. (1994). How permeable are clays and shales? *Water Resources Research*, 30(2), 145–150. <https://doi.org/10.1029/93WR02930>
- Neuzil, C. E. (2012). Hydromechanical effects of continental glaciation on groundwater systems. *Geofluids*, 12(1), 22–37. <https://doi.org/10.1111/j.1468-8123.2011.00347.x>
- Neuzil, C. E. (2013). Can shale safely host US nuclear waste? *Eos, Transactions American Geophysical Union*, 94(30), 261–262. <https://doi.org/10.1002/2013EO300001>
- Neuzil, C. E., & Person, M. (2017). Reexamining ultrafiltration and solute transport in groundwater. *Water Resources Research*, 53, 4922–4941. <https://doi.org/10.1002/2017WR020492>
- Neuzil, C. E., & Provost, A. M. (2014). Ice sheet load cycling and fluid underpressures in the Eastern Michigan Basin, Ontario, Canada. *Journal of Geophysical Research: Solid Earth*, 119, 8748–8769. <https://doi.org/10.1002/2014JB011643>
- Park, Y. J., Sudicky, E. A., & Sykes, J. F. (2009). Effects of shield brine on the safe disposal of waste in deep geologic environments. *Advances in Water Resources*, 32(8), 1352–1358. <https://doi.org/10.1016/j.advwatres.2009.06.003>
- Person, M., Bense, V., Cohen, D., & Banerjee, A. (2012). Models of ice-sheet hydrogeologic interactions: A review. *Geofluids*, 12(1), 58–78. <https://doi.org/10.1111/j.1468-8123.2011.00360.x>
- Person, M., Dugan, B., Swenson, J. B., Urbano, L., Stott, C., Taylor, J., & Willett, M. (2003). Pleistocene hydrogeology of the Atlantic continental shelf, New England. *Geological Society of America Bulletin*, 115(11), 1324–1343. <https://doi.org/10.1130/B25285.1>
- Person, M., McIntosh, J., Bense, V., & Remenda, V. H. (2007). Pleistocene hydrology of North America: The role of ice sheets in reorganizing groundwater flow systems. *Reviews of Geophysics*, 45, RG3007. <https://doi.org/10.1029/2006RG000206>
- Péwé, T. L. (1983). The periglacial environment in North America during Wisconsin time. *Late-quaternary Environments of the United States*, 1, 157–189.
- Roeloffs, E. A. (1988). Fault stability changes induced beneath a reservoir with cyclic variations in water level. *Journal of Geophysical Research*, 93(B3), 2107–2124. <https://doi.org/10.1029/JB093iB03p02107>
- Roeloffs, E. A. (1996). Poroelastic techniques in the study of earthquake-related hydrologic phenomena. In *Advances in Geophysics* (37, 135–195). Elsevier. DOI: [https://doi.org/10.1016/S0065-2687\(08\)60270-8](https://doi.org/10.1016/S0065-2687(08)60270-8)
- Rojstaczer, S. A., Ingebritsen, S. E., & Hayba, D. O. (2008). Permeability of continental crust influenced by internal and external forcing. *Geofluids*, 8(2), 128–139. <https://doi.org/10.1111/j.1468-8123.2008.00211.x>
- Scheidegger, A. E. (1961). General theory of dispersion in porous media. *Journal of Geophysical Research*, 66(10), 3273–3278. <https://doi.org/10.1029/JZ066i010p03273>
- Schlegel, M. E., Zhou, Z., McIntosh, J. C., Ballentine, C. J., & Person, M. A. (2011). Constraining the timing of microbial methane generation in an organic-rich shale using noble gases, Illinois Basin, USA. *Chemical Geology*, 287(1–2), 27–40. <https://doi.org/10.1016/j.chemgeo.2011.04.019>
- Sella, G. F., Stein, S., Dixon, T. H., Craymer, M., James, T. S., Mazzotti, S., & Dokka, R. K. (2007). Observation of glacial isostatic adjustment in “stable” North America with GPS. *Geophysical Research Letters*, 34, L02306. <https://doi.org/10.1029/2006GL027081>
- Siegel, D. I. (1991). Evidence for dilution of deep, confined ground water by vertical recharge of isotopically heavy Pleistocene water. *Geology*, 19(5), 433–436. [https://doi.org/10.1130/0091-7613\(1991\)019<0433:EFDODC>2.3.CO;2](https://doi.org/10.1130/0091-7613(1991)019<0433:EFDODC>2.3.CO;2)
- Siegel, D. I., & Mandle, R. J. (1984). Isotopic evidence for glacial meltwater recharge to the Cambrian-Ordovician aquifer, north-central United States. *Quaternary Research*, 22(03), 328–335. [https://doi.org/10.1016/0033-5894\(84\)90026-7](https://doi.org/10.1016/0033-5894(84)90026-7)
- Siegel, J., Person, M., Dugan, B., Cohen, D., Lizarralde, D., & Gable, C. (2014). Influence of late Pleistocene glaciations on the hydrogeology of the continental shelf offshore Massachusetts, USA. *Geochemistry, Geophysics, Geosystems*, 15, 4651–4670. <https://doi.org/10.1002/2014GC005569>
- Smith, L., & Chapman, D. S. (1983). On the thermal effects of groundwater flow: 1. Regional scale systems. *Journal of Geophysical Research*, 88(B1), 593–608. <https://doi.org/10.1029/JB088iB01p00593>
- Steffen, R., Wu, P., Steffen, H., & Eaton, D. W. (2014). The effect of earth rheology and ice-sheet size on fault slip and magnitude of postglacial earthquakes. *Earth and Planetary Science Letters*, 388, 71–80. <https://doi.org/10.1016/j.epsl.2013.11.058>
- Stein, R. S. (1999). The role of stress transfer in earthquake occurrence. *Nature*, 402(6762), 605–609. <https://doi.org/10.1038/45144>
- Stein, R. S., King, G. C., & Lin, J. (1992). Change in failure stress on the southern San Andreas fault system caused by the 1992 magnitude = 7.4 Landers earthquake. *Science*, 258(5086), 1328–1332. <https://doi.org/10.1126/science.258.5086.1328>
- Stein, R. S., King, G. C., & Lin, J. (1994). Stress triggering of the 1994 $M = 6.7$ Northridge, California, earthquake by its predecessors. *Science*, 265(5177), 1432–1435. <https://doi.org/10.1126/science.265.5177.1432>

- Stober, I., & Bucher, K. (2007). Hydraulic properties of the crystalline basement. *Hydrogeology Journal*, 15(2), 213–224. <https://doi.org/10.1007/s10040-006-0094-4>
- Talbot, C. J. (1999). Ice ages and nuclear waste isolation. *Engineering Geology*, 52(3–4), 177–192. [https://doi.org/10.1016/S0013-7952\(99\)00005-8](https://doi.org/10.1016/S0013-7952(99)00005-8)
- Tarasov, L., & Peltier, W. R. (2007). Coevolution of continental ice cover and permafrost extent over the last glacial-interglacial cycle in North America. *Journal of Geophysical Research*, 112, F02S08. <https://doi.org/10.1029/2006JF000661>
- Timoshenko, S. P., & Goodier, J. N. (1970). *Theory of elasticity* (Vol. 3, pp. 403–408). London: McGraw-Hill, New York.
- Townend, J., & Zoback, M. D. (2000). How faulting keeps the crust strong. *Geology*, 28(5), 399–402. [https://doi.org/10.1130/0091-7613\(2000\)28<399:HFKTCS>2.0.CO;2](https://doi.org/10.1130/0091-7613(2000)28<399:HFKTCS>2.0.CO;2)
- Turcotte, D., & Schubert, G. (2001). *Geodynamics*. New York: Cambridge University Press.
- Van der Veen, C. J. (1999). *Fundamentals of glacier dynamics*. Boca Raton, FL: CRC Press.
- Vinard, P., Blümling, P., McCord, J. P., & Aristorenas, G. (1993). Evaluation of hydraulic underpressures at Wellenberg, Switzerland. *International Journal of Rock Mechanics and Mining Sciences & Geomechanics Abstracts*, 30(7), 1143–1150. Pergamon
- Vinard, P., Bobet, A., & Einstein, H. H. (2001). Generation and evolution of hydraulic underpressures at Wellenberg, Switzerland. *Journal of Geophysical Research*, 106(B12), 30,593–30,605. <https://doi.org/10.1029/2001JB000327>
- Voller, V. R. (2009). *Basic control volume finite element methods for fluids and solids* (Vol. 1). Singapore: World Scientific. <https://doi.org/10.1142/7027>
- Walcott, R. I. (1970). Flexural rigidity, thickness, and viscosity of the lithosphere. *Journal of Geophysical Research*, 75(20), 3941–3954. <https://doi.org/10.1029/JB075i020p03941>
- Walker, J. C., & Kasting, J. F. (1992). Effects of fuel and forest conservation on future levels of atmospheric carbon dioxide. *Palaeogeography, Palaeoclimatology, Palaeoecology*, 97(3), 151–189. [https://doi.org/10.1016/0031-0182\(92\)90207-L](https://doi.org/10.1016/0031-0182(92)90207-L)
- Walsh, R. (2011). Compilation and consolidation of field and laboratory data for hydrogeological properties. Geofirma Engineering Ltd. Tech. Rep. TR-08, 10, 28.
- Walsh, R., Calder, N., & Avis, J. (2012). A simple implementation of 1D hydromechanical coupling in TOUGH2. In *Proceedings of the TOUGH Symposium* (pp. 425–432). Berkeley, CA: Lawrence Berkeley National Laboratory.
- Walvoord, M. A., Voss, C. I., & Wellman, T. P. (2012). Influence of permafrost distribution on groundwater flow in the context of climate-driven permafrost thaw: Example from Yukon Flats Basin, Alaska, United States. *Water Resources Research*, 48, W07524. <https://doi.org/10.1029/2011WR011595>
- Wang, C. Y., Liao, X., Wang, L. P., Wang, C. H., & Manga, M. (2016). Large earthquakes create vertical permeability by breaching aquitards. *Water Resources Research*, 52, 5923–5937. <https://doi.org/10.1002/2016WR018893>
- Wang, H. F., & Anderson, M. P. (1982). *Introduction to groundwater modeling: Finite difference and finite element methods*. San Diego, CA: Academic Press.
- Wheeler, R. L., & Cramer, C. H. (2002). Updated seismic hazard in the southern Illinois basin: Geological and geophysical foundations for use in the 2002 USGS national seismic-hazard maps. *Seismological Research Letters*, 73(5), 776–791. <https://doi.org/10.1785/gssrl.73.5.776>
- Wood, R. M. (1989). Extraordinary deglaciation reverse faulting in northern Fennoscandia. In *Earthquakes at North-Atlantic passive margins: Neotectonics and postglacial rebound* (pp. 141–173). Dordrecht: Springer. https://doi.org/10.1007/978-94-009-2311-9_10
- Wu, P. (1992). Deformation of an incompressible viscoelastic flat earth with powerlaw creep: A finite element approach. *Geophysical Journal International*, 108(1), 35–51. <https://doi.org/10.1111/j.1365-246X.1992.tb00837.x>
- Wu, P. (2004). Using commercial finite element packages for the study of earth deformations, sea levels and the state of stress. *Geophysical Journal International*, 158(2), 401–408. <https://doi.org/10.1111/j.1365-246X.2004.02338.x>
- Wu, P. (2013). *Estimation of maximum horizontal rebound stresses at 850 m depth below Bruce nuclear site, NWMO Technical Memorandum* (p. 18). Calgary, Canada: University of Calgary.
- Wu, P., & Hasegawa, H. S. (1996). Induced stresses and fault potential in eastern Canada due to a realistic load: A preliminary analysis. *Geophysical Journal International*, 127(1), 215–229. <https://doi.org/10.1111/j.1365-246X.1996.tb01546.x>
- Zheng, C., & Bennett, G. D. (1995). *Applied contaminant transport modeling: Theory and practice*. New York: Wiley.
- Zoback, M. D., & Townend, J. (2001). Implications of hydrostatic pore pressures and high crustal strength for the deformation of intraplate lithosphere. *Tectonophysics*, 336(1–4), 19–30. [https://doi.org/10.1016/S0040-1951\(01\)00091-9](https://doi.org/10.1016/S0040-1951(01)00091-9)
- Zoback, M. L., & Zoback, M. D. (1989). Tectonic stress field of the continental United States. *Geophysical framework of the continental United States: Geological Society of America Memoir*, 172, 523–539.